M 2022

U.PORTO
FEUP FACULDADE DE ENGENHARIA
UNIVERSIDADE DO PORTO

DETERMINATION OF PARTICLE AGGLOMERATION ZONES DURING COUNTER-CURRENT SPRAY DRYING USING CFD SIMULATION

VANESSA ELIANA MENDES

MASTER THESIS IN CHEMICAL ENGINEERING
PRESENTED TO THE FACULTY OF ENGINEERING
OF THE UNIVERSITY OF PORTO

Master's in chemical engineering

Determination of particle agglomeration zones during counter-current spray drying using CFD simulation

Master dissertation

of

Vanessa Eliana Mendes

Developed within the course of dissertation

held in

Lodz University of Technology

Lodz University of Technology
Faculty of Process and Environmental Engineering

Supervisor at FEUP: **Prof. Manuel Alves**

Coordinator at Lodz University of Technology: **Dr. Maciej Jaskulski**

U.PORTO
FEUP FACULDADE DE ENGENHARIA
UNIVERSIDADE DO PORTO

DEPARTAMENTO DE
ENGENHARIA QUÍMICA

July 2022

Acknowledgment

I'd want to express my gratitude to everyone who assisted me in writing this master’s thesis.

A special thanks:

To FEUP for being my home while I pursued my master's degree.

To Lodz University of Technology for accepting me as an intern.

To Maciej Jaskulski for supervising this thesis, for all the knowledge transmitted and for all the good conversations about the history of the world.

To my co-worker Dawid Zawadski, for all availability, friendliness and understanding on Monday mornings.

To Professor Manuel Alves for accepting the invitation to be my supervisor and for the dedication and availability in reviewing this dissertation.

To Process and Environmental Department, a warm thanks for receiving me with open arms and always with such kindness.

To my gold friends and new friends from Łódź, who made this journey even beauty.

To my family for holding on to the longing and always having the right words.

To my mom, for all the strength.

To Cláudio, for being my everyday support.

Abstract

Counter current spray dryers, although very efficient, are poorly understood due to the complex agglomeration phenomenon that occurs during operation. Experimentally there is no reliable method to predict agglomeration. Mathematical models have been applied for this purpose, but the lack of experimental results prevents the verification of the models.

In this study, modelling of a two-nozzle counter-current spray drying process using Computational Fluid Dynamics (CFD) simulation is presented in order to determine the agglomeration zones.

Information about the glass transition temperature (T_g) of the particles inside the dryer can be used to determine agglomeration zones caused by stickiness of the particles. Gordon-Taylor equation allows to determine T_g as a function of moisture content of the particles. A comprehensive moisture evaporation model based on the Characteristic Drying Curve (CDC) was applied to describe the drying kinetics of a 40 % (w/w) maltodextrin dextrose equivalent 12 (DE12) aqueous solution.

In order to determine particle characteristics in each position, a Discrete Phase Model (DPM) was also implemented. These models where developed using C language and implemented on Ansys Fluent by means of User Defined Functions (UDF). Changes on particle moisture content, temperature and position were followed and these values, together with T_g, were used to determine possible agglomeration zones inside the drying chamber.

The drying process was simulated in transient state. The instability of the flow in the geometry was corroborated by examining velocity and temperature profiles. The similarity between the radial temperature profiles obtained experimentally and through CFD allow to accurately estimate particle temperature. Maltodextrin DE12 was shown to be more probable to aggregate towards the chamber's bottom, where temperatures are higher and moisture content levels are lower. For higher flow rates it was verified that there are more places that are prone to cause agglomeration. When the inlet temperature is high, the product degrades and becomes a yellowish powder. Despite the results obtained through simulation, this model still requires experimental validation.

Keywords: Counter-current spray dryer, CFD simulation, Particles stickiness, Agglomeration, Glass transition temperature

Resumo

Os secadores de spray em contra corrente, apesar de muito eficientes, são ainda pouco entendidos devido ao complexo fenómeno de aglomeração que ocorre durante a sua operação. Experimentalmente não existe um método adequado para prever a formação de aglomerados. Métodos matemáticos têm sido aplicados para este efeito, mas a escassez de resultados experimentais impede a verificação dos modelos.

Neste estudo, efetuou-se a simulação de um processo de secagem por pulverização em contracorrente munido com dois injetores, utilizando ferramentas de dinâmica de fluidos computacional, com vista a determinar as zonas em que a aglomeração ocorre.

Informações sobre a temperatura de transição vítrea (T_g) das partículas dentro do secador podem ser utilizadas para determinar zonas de aglomeração causadas por partículas pegajosas. A equação de Gordon-Taylor permite determinar a T_g em função do teor de humidade das partículas. Um modelo de evaporação da humidade baseado na curva característica de secagem foi utlizado para descrever a cinética de secagem de uma solução aquosa a 40% (p/p) de maltodextrina com dextrose equivalente 12 (DE12). Com vista a determinar as caraterísticas das partículas em cada posição, foi também implementado um modelo de fase discreta. Estes modelos foram desenvolvidos utilizando a linguagem C e implementados no Ansys Fluent através de funções definidas pelo utilizador (UDF). Alterações no teor de humidade das partículas, temperatura e posição foram guardados, juntamente com a T_g, e foram utilizados para determinar possíveis zonas de aglomeração dentro da câmara de secagem.

O processo de secagem foi simulado em estado transiente. Os perfis de velocidade e temperatura foram analisados, demonstrando a instabilidade do escoamento na geometria.

A comparação entre os perfis radiais de temperatura obtidos experimentalmente e utilizando CFD mostram boa concordância, permitindo estimar corretamente a temperatura das partículas.

Constatou-se que a maltodextrina DE12 é mais propensa a aglomerar no fundo da câmara onde as temperaturas são mais elevadas e a humidade é mais reduzida. Caudais mais elevados apresentam um maior número de zonas de aglomeração e temperaturas de entrada demasiado elevadas causam degradação do produto, alterando a sua cor para um tom amarelado.

Apesar dos resultados obtidos através de simulação serem vitais, este modelo ainda requer validação experimental.

Palavras-chave: Secagem por pulverização em contra corrente, Simulação com CFD, Aderência das partículas, Aglomeração, Temperatura de transição vítrea

Declaration

I hereby declare, under word of honour, that this work is original and that all non-original contributions are indicated, and due reference is given to the author and source

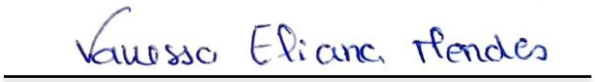

Vanessa Eliana Mendes

3rd July 2022

Index

List of Figures

List of Tables

Notation and Glossary

A	surface area	m^2
C	molar vapour concentration	$mol\,m^{-3}$
C_D	drag coefficient	-
c_P	specific heat	$J\,kg^{-1}\,K^{-1}$
d	diameter	m
D	diffusion coefficient	$m^2\,s^{-1}$
F	force	N
f	drying rate coefficient	$kg\,m\,s^{-2}$
g	gravitational acceleration	$m\,s^{-2}$
h	sensible enthalpy	$J\,kg^{-1}$
ΔH_{vap}	latent heat of evaporation	$J\,kg^{-1}$
k	turbulent kinetic energy	$m^2\,s^{-2}$
K	solute–water binary constant	-
m	mass	kg
M	molar mass	$kg\,kmol^{-1}$
$\dot{m}$	mass flow rate	$kg\,s^{-1}$
p	partial pressure	Pa
Q	heat transfer	W
R	universal gas constant	$J\,K^{-1}\,mol^{-1}$
S	actual surface area of the particle	m^2
s	surface of a sphere with the same volume as the particle	m^2
S_f	momentum source term	$N\,m^{-3}$
S_m	mass source term	$kg\ m^{-3}\,s^{-1}$
S_h	heat source term	$W\,m^{-3}$
T	temperature	°C
t	time	s
ΔT_{lm}	mean logarithmic temperature difference	°C
T_g	glass transition temperature	°C
v	velocity	$m\,s^{-1}$
x	typical cell size	-
X	moisture content (kg_{water}/kg_{solid})	-
y	weight fraction	-

Greek Letters

α	heat transfer coefficient	$W\,m^{-2}\,K^{-1}$
β	mass transfer coefficient	$m\,s^{-1}$
ε	turbulence dissipation rate	$m^2\,s^{-3}$
λ	heat conductivity	$W\,m^{-1}\,K^{-1}$
μ	dynamic viscosity	$kg\,m^{-1}\,s^{-1}$
μ_T	eddy viscosity	$kg\,m^{-1}\,s^{-1}$
ρ	density	$kg\,m^{-3}$
ϕ	particle sphericity	-
Ω	specific turbulence dissipation rate	s^{-1}

Subscripts

amb	ambient
cr	critical
eq	equilibrium
f	fluid
in	inlet
op	operation

out	outlet
p	particle/droplet
s	solute
sat	saturation
sur	surface
t	turbulent
vap	vapour
w	water

List of acronyms

3D	Three Dimensional
CDC	Characteristic Drying Curve
CFD	Computational Fluid Dynamics
DE	Dextrose Equivalent
DNS	Direct Numerical Simulation
DSC	Differential Scanning Calorimeter
DPM	Discrete Phase Model
LES	Large Eddy Simulation
LDA	Laser Doppler Anemometry
N-S	Navier-Stokes equation
PSD	Particle Size Distribution
PSI-Cell	Particle-Source-In Cell
RANS	Reynolds-Averaged Navier-Stokes
REA	Reaction Engineering Approach
SKE	Standard k-ε model
UDF	User Defined Function

Dimensionless numbers

Co	Courant number, $Co = \frac{v\Delta t}{\Delta x}$
Re	Reynolds number, $\mathrm{R_e} = \frac{v\, d\rho}{\mu}$
$\mathrm{Pr_t}$	Prandtl number, $\mathrm{P_r} = \frac{c_P \mu}{\lambda}$
Sc	Schmidt number, $\mathrm{S_c} = \frac{\mu}{\rho D}$

1 Introduction

A spray dryer is an equipment designed to produce powders by drying small droplets of solution with a hot gas stream. Counter-current spray drying towers are thermally more efficient than co-current ones due to the interaction between the two phases. However, the intense mixing that occurs during counter-current processes increases the complexity of the flow in terms of kinetics and collisions between particles. Collisions have a significant impact on the final product, since they promote coalescence and agglomeration, causing uncontrollable changes in particle size and morphology.

Agglomeration is seen as one of the biggest challenges in counter-current systems, especially when dealing with sugars which stickiness leads to agglomeration. When the objective is to produce small and uniform particles, agglomeration is seen as a limitation, especially if it leads to operational problems. On the other hand, if the final product specifications require larger dimensions, stickiness can be used to achieve agglomeration inside the chamber.

Due to the complexity of the flow, the number of counter-current systems are limited. Furthermore, there are still no reliable measuring devices capable of characterizing morphological changes in particles during the drying process. As a result, there is no way to forecast this agglomeration, making the empirical research of this phenomenon extremely challenging.

Following this, to understand this phenomenon, numerical modelling using Computational Fluid Dynamics (CFD) is often used. In this program, a 2D or 3D model of the spray dryer is created to reflect the geometry under study. Subsequently, models can be included in order to recreate the conditions in the spray dryer process as real as possible. However, the lack of studies and experimental results regarding counter-current configurations difficults the verification of mathematical models to determine agglomeration during drying.

In this dissertation, a pilot-plant of a counter-current spray dryer powered by two nozzles at two different heights, located at the Lodz University of Technology in Poland, is simulated in Ansys Fluent program (version 2022 R1). CFD simulation of the dryer process was performed in order to determine particle agglomeration zones for a 40% (w/w) aqueous maltodextrin DE12 solution. For this purpose, models to track particles position, properties and to monitor drying process were used to determine the glass transition temperature (T_g). Afterwards, a relation between T_g and stickiness were used to identify the sticky regions inside the chamber that are responsible for agglomeration in sugars.

1.1 Aim of dissertation

The aim of this dissertation is to determine the particle agglomeration zones in a two-nozzle spray dryer tower using CFD simulation.

In the first chapter, the challenges regarding spray drying agglomeration were discussed and a solution using CFD simulation was proposed.

The second chapter provides a brief overview of spray drying process and present the models implemented as a UDF in the Fluent code for prediction of agglomeration zones:

- Discrete Phase Model (DPM);
- Characteristic Drying Curve (CDC);
- Gordon-Taylor equation.

In the third chapter, the spray drying installation under study is described. The discretization process of the geometry generated in Ansys program is displayed. The boundary conditions are defined, and the heat losses model is presented and verified.

In chapter four, the results obtained from modelling are presented and discussed. In addition, some results are compared to those obtained by experiments.

Chapter five summarizes this dissertation, concludes the research work findings and present recommendations for future work.

2 Context and State of the art

2.1 Spray drying

Spray drying is a unit operation that consists in the thermal dehydration of wet materials to produce dry powders. It is extensively used in food products, detergents, pharmaceutical industry, ceramics and agrochemicals to decrease product weight and to prevent materials from biological deterioration (Jaskulski et al., 2018; Verdurmen et al., 2006).

This process has the advantage of being a simple, versatile and suitable method for upscaling systems (Gecim & Kalemtas, 2021). The main disadvantages include the high capital cost, low thermal efficiency, when heat recovery methods are not adopted, and relatively large volume of the drying chamber (Kudra & Strumillo, 1998).

This process includes atomizing small droplets (150 - 500 µm) of a solution, slurry or paste into a chamber along with a gas stream preheated in an external heating system. When droplets get into contact with the gas stream, moisture is evaporated and leaves the dryer with exhaust gas. At the bottom, the dried product is received as a powder (Kudra & Strumillo, 1998).

There are three types of spray dryer configurations: co-current, counter-current and mixed flow, where those mentioned last are used the least (Figure 1). Each configuration leads to production of powders with different morphological and physical properties.

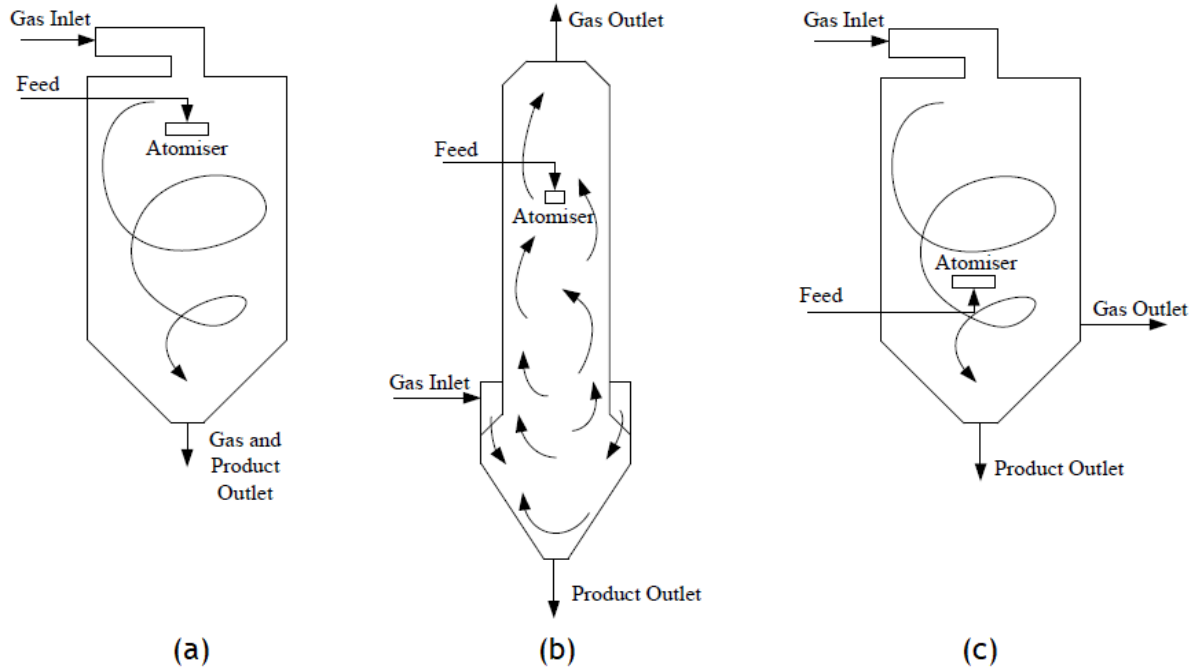

Figure 1 Spray dryer diagrams: (a) Co-current flow; (b) Counter-current flow; (c) Mixed flow. Adapted from Ali (2014).

Co-current spray dryers spread both gas and slurry at the same side, typically at the top of the drying chamber (Kudra & Strumillo, 1998). This process is simpler than the others and useful for thermal sensitive materials, such as food and pharmaceutical products. In counter-current spray drying, the material to dry and the drying gas are injected at opposite locations in the drying chamber. This system is mainly applied to thermally stable products, such as detergent powder and chemical fertilizers (Ali, 2014; Jaskulski, 2015).

Counter-current configurations are thermally more efficient than co-current due to the intensive mixing of discrete phase (droplets/particles) and continuous phase (drying gas) (Ali, 2014). In addition, these systems allow drying of sticky products, intensify agglomeration to increase particle diameter or reduce dust, high yields, and multiple spray stages, resulting in superior overall economics (Zbicinski & Piatkowski, 2009).

Despite being more efficient, counter-current systems are far more complex in terms of flow hydrodynamics than co-current processes. In co-current processes, recirculation between air and particle is minimal due to the parallel phase flow, limiting agglomeration and wall deposition (Jaskulski et al., 2018). On the contrary, in counter-current systems, the intensive mixing of two phases favours recirculation and agglomeration of discrete phase (Zbicinski & Piatkowski, 2009).

According to Zbicinski and Piatkowski (2009), counter-current spray drying is a poorly understood process. Due to the complexity of the process, there are few counter-current facilities under research. In addition, the ongoing research is done by big companies (e.g., Henkel, Tetra Pak, Procter and Gamble Polska), that do not share the results or hide pertinent information hindering future researches (Jaskulski, 2015; Zbicinski & Piatkowski, 2009). Studies on the kinetics of this equipment would help control phenomena such as agglomeration, wall deposition and thermal degradation of the product by controlling operating conditions and tower design (Ali, 2014).

Among all the topics, agglomeration is the key phenomenon that needs to be better understood and controlled to make the process easier to control (Zbicinski & Piatkowski, 2009). The ability to predict agglomeration could help in the prevention of operational issues (e.g., fouling of the dryer), in the prevention of agglomeration when the objective is to produce small and uniform particles or be used to perform agglomeration to adjust final powder properties (Gianfrancesco et al., 2010).

One impasse to achieve this lies in the fact that the existing measurement systems do not allow to morphologically characterize the particles during the drying, making it hard to study phenomena such as agglomeration or coalescence that have such a large impact on the final product of these systems (Zbicinski & Piatkowski, 2009).

As a way of overcome these issues, mathematical modelling using CFD has been used in this field due to its high potential to predict spray dryer performance by analysing the droplet, particles, gas and wall interactions (Ali, 2014).

The use of simulation techniques turns out to be more time and cost effective than experiments (Jaskulski et al., 2018). For different chamber designs and raw materials used, the operating conditions of a spray dryer vary (Malafronte et al., 2015). Therefore, without simulation tools, the approach used to optimise operating conditions for each process and also adjust the spray nozzle position to, for example, control agglomeration, was through "trial and error" (Verdurmen et al., 2004). Therefore, simulation tools are required in order to save time and money while improving the final product's quality.

Modelling spray drying process using 3D CFD simulation allows to analyse local changes of continuous and disperse phases along the drying process, as well as particle properties and morphology (Jaskulski, 2015). In addition, CFD simulation has been used as an attempt to predict agglomeration phenomenon.

2.2 Computational Fluid Dynamics (CFD)

CFD is a tool based on numerical calculations for solving problems related to fluids. The working method includes solving numerically the Navier-Stokes (N-S) equation of momentum, mass and energy conservation, Equations (1) to (3) (Ferziger & Peric, 2002). This method allows the analysis of local changes and provides local distributions of temperature, turbulence intensity, pressure and velocity inside the drying chamber (Woo, 2016).

The momentum conservation can be described as:

$$\rho\left(\frac{\mathrm{d}\vec{v}}{\mathrm{d}t}+\vec{v}\cdot\nabla\vec{v}\right)=-\nabla p+(\mu+\mu_t)\nabla^2\vec{v}+\rho\vec{g}+\overrightarrow{S_f} \tag{1}$$

where $\vec{v}$ stands for the velocity vector of the fluid, t for time, p for the static pressure, μ for dynamic viscosity, μ_t for turbulent viscosity, ρ for density and g for gravitational acceleration.

Mass and energy conservation have also to be considered in the simulation of drying process, in order to determine the temperature and humidity distribution. The mass conservation is given by:

$$\frac{\mathrm{d}\rho}{\mathrm{d}t}+\nabla(\rho\vec{v})=S_m \tag{2}$$

and the energy conservation can be written as:

$$\frac{d}{dt}(\rho h)+\nabla(\rho h\vec{v})=\nabla[(\lambda+\lambda_t)\nabla T]+S_h \tag{3}$$

where T is the temperature, h the sensible enthalpy and λ the heat conductivity.

In Equations (1) to (3), S_f, S_m, and S_h, represent additional sources of momentum, mass and heat that may exist inside the computing cell.

The sensible enthalpy is calculated from (Ferziger & Peric, 2002):

$$h = \int_{T_{ref}}^{T} c_P \, \mathrm{d}T \tag{4}$$

while heat conductivity due to turbulent transport, λ_T, is calculated from (Ferziger & Peric, 2002):

$$\lambda_t = \frac{c_P \mu_t}{\mathrm{Pr}_t} \tag{5}$$

where Pr_t is the Prandtl number (Ferziger & Peric, 2002) and c_P the specific heat of the fluid.

Drying processes are characterized by high turbulence caused by fluid swirls that moves chaotically inside the chamber. This turbulence generates forces and stresses that can be mathematically described using the turbulent viscosity. In order to solve the N-S equations, a turbulence model will be employed to determine turbulent viscosity (Ferziger & Peric, 2002).

2.2.1 Turbulence modelling

For turbulent flows, a turbulence model is required in order to solve the N-S equations. There are different turbulence models that can be used depending on the scale of turbulent eddies and available computational resources. Direct Numerical Simulation (DNS) is an approach that allows to solve directly N-S equations without using additional modelling assumptions. However, this method is not capable to simulate flows in large geometries due to excessive computational requirements (Ali, 2014). Reynolds Average Navier-Stokes equations (RANS) is the most widely used turbulence approach for industrial flows. This model allows to solve time-averaged N-S equations, by doing approaches in the level of details in the turbulence prediction (Woo, 2016). Another approach for modelling turbulence is the Large Eddy Simulation (LES), where the large-scale eddies are numerically solved, and the small eddies are modelled using RANS method. Comparing to RANS, this method needs more computational power, being more expensive (Ali, 2014). Therefore, the RANS method was chosen for CFD modelling of this drying chamber.

There are many RANS turbulence models available in Ansys Fluent, such as $k-\varepsilon$, $k-\Omega$, and modifications of them. The standard $k-\varepsilon$ model (SKE) is the most used turbulence model for industrial purposes, due to its simplicity and flexibility in modelling a wide range of turbulent flows in a region away from the walls (Ali, 2014; Jaskulski, 2015). This model is considered numerically robust and reasonably accurate for the required computational resources (Jubaer et al., 2019).In the standard $k-\varepsilon$ model, k stands for turbulent kinetic

energy and ε represents the turbulence dissipation rate (Ali, 2014). The introduction of these two variables allows the N-S equations to be solved.

In the *k-Ω* model, Ω stands for specific rate of dissipation, and calculations are carried out in a simple and stable way. This model allows a better description of the fluid in the vicinity of the wall when compared with the $k-\varepsilon$ model. On the other hand, the $k-\Omega$ model strongly depends on the specified value of Ω, a limitation which is not observed using the $k-\varepsilon$ model (Jubaer et al., 2019).

In the simulations, the convergence criteria for both turbulence models are specified as 1×10^{-3} for continuity, turbulence model and momentum equations.

Both $k-\varepsilon$ and $k-\Omega$ turbulence models were tested. Using the *k-Ω* model does not allow to achieve a convergent solution. On the other hand, convergence was reached using the $k-\varepsilon$ model, showing good agreement with experimental data.

Thus, standard $k-\varepsilon$ model was adopted and can be described by Equations (6) and (7) (Launder & Spalding, 1974):

$$\rho\frac{dk}{dt}=\frac{\partial}{\partial x}\left[\left(\mu+\frac{\mu_t}{\sigma_k}\right)\frac{\partial k}{\partial x}\right]+G_k+G_b-\rho\varepsilon-Y_M+S_k \tag{6}$$

$$\rho\frac{d\varepsilon}{dt}=\frac{\partial}{\partial x}\left[\left(\mu+\frac{\mu_t}{\sigma_\varepsilon}\right)\frac{\partial \varepsilon}{\partial x}\right]+G_{1\epsilon}\frac{\varepsilon}{k}(G_k+C_{3\varepsilon}G_b)-C_{2\varepsilon}\rho\frac{\varepsilon^2}{k}+S_\varepsilon \tag{7}$$

These equations will be solved to determine the turbulent viscosity (μ_t) in order to solve N-S equations (Launder & Spalding, 1974):

$$\mu_t=0.09\rho\frac{k^2}{\varepsilon} \tag{8}$$

The choice of turbulence model is of high importance since it influences the flow field prediction (Jubaer et al., 2019). Also, depending on whether the process variables change over time or not, a different turbulence model can be applied. An unsteady state is adopted when parameters at different locations start to show significant fluctuations. For counter-current spray dryer this state is expected when particle injection is added into a steady flow field, once it instigates fluctuations (Jubaer et al., 2019).

2.2.2 Implementation of Discrete Phase Model (DPM)

In order to determine particle characteristics, it is necessary to implement the Discrete Phase Model (DPM). The DPM model is based on Particle-Source-In Cell (PSI-CELL) method (Razmi et al., 2021). This method begins with the calculation of the velocity distribution field of the continuous phase by solving the N-S equations. Then, particles are injected and changes in the velocity of the continuous phase are analysed and allow to determine the trajectory of the particles and their impact on the continuous phase parameters (Jaskulski et al., 2018).

In the DPM model, groups of particles are treated as streams that are tracked until they leave the computational domain. In each DPM iteration, the position of each particle is updated. Initially, the trajectory of the particles is calculated based on the previous step. Following that, the trajectory of the segment end is determined by balancing the forces acting on them (Jaskulski et al., 2018), as expressed in the following force balance (Jaskulski, 2015):

$$\frac{dv_p}{dt} = F_{drag} + F_{gravity} = \frac{18\mu}{\rho_p d_p^2}\frac{C_D \mathrm{Re}}{24}\left(v_f - v_p\right) + \frac{g\left(\rho_p - \rho_f\right)}{\rho_p} \tag{9}$$

where d_p stands for particle diameter, Re for Reynolds number (Ferziger & Peric, 2002), C_D for drag coefficient and the subscripts *p* and *f* refer to particle and fluid, respectively.

For this balance only drag force and gravity are considered, since these terms have the most influence in the force balancing. Due to small size of the particles, other forces can be neglected since removing them the particle trajectory remains the same.

The drag coefficient depends on velocity and shape of the particle and on the properties of the medium in which it moves. This coefficient can be determined following the correlation proposed by Haider & Levenspiel (1989), which is valid for particle *Re* ranging from 0.1 to 10^5, and is given by:

$$C_D = \frac{24}{\mathrm{Re}}\left(1 + A\ \mathrm{Re}^B\right) + \frac{C}{1 + \frac{D}{\mathrm{Re}}} \tag{10}$$

where the coefficients *A, B, C* and *D* can be determined from the following equations, using the particle sphericity(ϕ) (Haider & Levenspiel, 1989):

$$A = \exp\left(2.3288 + 6.4581\phi + 2.4486\phi^2\right) \tag{11}$$

$$B = 0.0964 + 0.5565\phi \tag{12}$$

$$C = \exp\left(4.905 - 13.8944\phi + 18.4222\phi^2 - 10.2599\phi^3\right) \tag{13}$$

$$D = \exp\left(1.4681 + 12.2584\phi - 20.7322\phi^2 + 15.8855\phi^3\right) \tag{14}$$

$$\phi = \frac{s}{S} \tag{15}$$

where S is the actual surface area of the particle and s is the surface of a sphere with the same volume as the particle (Haider & Levenspiel, 1989).

Based on the particle velocity determined from the force balance, Equation (9), together with the information on the length that particle has moved, it is possible to determine the time that a particle needs to move through all the segment (DPM time step) (Jaskulski et al., 2018).

When all stream trajectories are calculated, the mass and heat balance between the particle streams and the surrounding air is solved. Based on this, the new profiles of pressure, velocity and temperature are updated and used for the next DPM iteration. This procedure is repeated

until the solution converges. The information about particles position, diameter, moisture content and temperature is saved in memory for further calculations (Jaskulski et al., 2018).

The total heat transfer through the tower can be described by:

$$Q = \dot{m}_P c_P (T_{in} - T_{out}) \tag{16}$$

where $\dot{m}_P$ is the mass flow rate of the slurry.

The heat transfer by convection from air to the particles can be determined using the following equation:

$$Q = A_p \alpha_p \left(T_{amb} - T_p\right) \tag{17}$$

where A_p is the area of the particle and α_p the convective heat transfer coefficient.

Once the temperature of the air changes throughout the tower, a mean logarithmic temperature difference (ΔT_{lm}) will be used in Equation (17).

The heat transfer from the particles to air is a function of the evaporation rate of drying and is given by:

$$Q = -\Delta H_{vap} \frac{dm_p}{dt} \tag{18}$$

were ΔH_{vap} is the latent heat of evaporation.

Therefore, the change in the particle temperature can be determined using the energy balance (Woo, 2016):

$$\frac{dT_p}{dt} = \frac{A_p \alpha_p \left(T_{amb} - T_p\right) + \Delta H_{vap} \frac{dm_p}{dt}}{\dot{m}_P c_P} \tag{19}$$

The heat transfer by radiation is neglected in the energy balance.

Considering droplets/particles as perfect homogeneous spheres, the heat transfer coefficient can be determined from the Ranz Marshal correlation (Wawrzyniak et al., 2017):

$$\alpha_p = \frac{\lambda_f}{d_p}\left(2.0 + 0.6\mathrm{Re}_p^{\frac{1}{2}}\,\mathrm{Pr}^{\frac{1}{3}}\right) \tag{20}$$

The CFD program requires the implementation of external codes when some models are not available in commercial CFD codes. Thereby, some models will be incorporated into CFD simulation using User-Defined Function (UDF) written in C language. The UDF named "DEFINE_DPM_HEAT_AND_MASS" from Ansys will be employed with some modifications in the Fluent program to specify the heat and mass transfer of multicomponent particles to the gas phase (Appendix A). The evaporation rate of drying from the energy balance will be determine resorting to the particle drying model.

2.2.3 Particle drying models

Mass transfer between the droplets/particles and the surrounding air must be determined in order to correctly describe the drying process. Reaction Engineering Approach (REA) and Characteristic Drying Curve (CDC) are the most commonly used particle drying mathematical models for spray drying processes. In both methods, the change in temperature distribution inside the droplet/particle is not considered. In addition, both models are simple and neither requires much computational resources (Ali, 2014).

CDC model is based on changes in drying rate as a function of moisture content (X) of the material. One limitation of this model is that the critical moisture content (X_{cr}) is considered to be constant, but it may vary with surrounding air conditions (Ali, 2014).

On the other hand, in the REA model for the evaporation process to happen, an energy activation barrier must be overcome. This approach requires an empirical correlation relating the partial vapour concentration over the droplet/particle with the average moisture content. One advantage of this model is that it does not require the critical moisture content which may vary with the drying conditions (Ali, 2014).

Both models are suitable for description of drying model. CDC model will be applied once there is available information about maltodextrin DE12 drying process.

CDC model is based on the assumption of two periods of drying, a constant rate of drying period followed by a falling drying rate period. Typical droplet temperature and moisture content evolutions during drying process are shown in Figure 2.

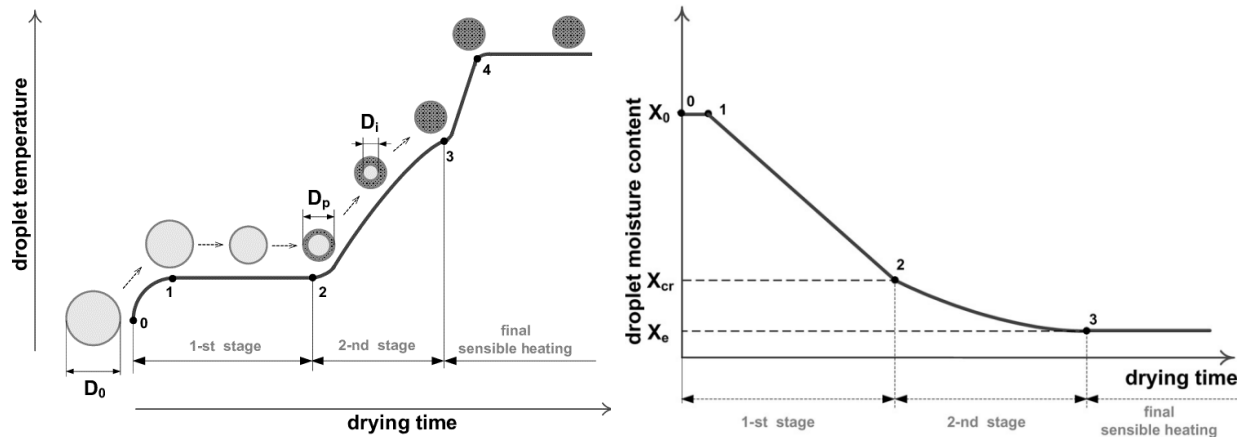

(a) (b)

Figure 2 Two-stage droplet drying kinetics over time: (a) droplet/particle temperature; (b) moisture content (Borde, 2010).

In the first stage, the droplet is exposed to drying gas and begins to heat until it achieves a constant temperature, called wet bulb temperature (Figure 2 (a); points 0-1). With continuous heating, droplet starts evaporating from the surface (Figure 2 (a); points 1-2). During this phase, the drying rate is constant and has the highest value in all the process. This step results in the shrinkage of the droplet diameter. When the moisture excess is completely evaporated, a solid crust begins to form on its surface. At this moment, the droplet transforms into a wet particle and the second drying stage begins (Figure 2 (a); point 2). This point is called "locking point" and corresponds to the critical moisture content (X_{cr}). In the second stage, the crust layer provides additional resistance to mass transfer, leading to a drop of the drying rate. With the growth in drying time, the moisture content inside the particle reduces, increasing the particle's temperature, the surrounding solid crust and consequently the diffusion resistance inside de particle (Figure 2 (a); points 2-3). The second drying stage continues until the particle moisture content is reduced to equilibrium (X_{eq}). After that, the particle is dried almost completely and then warmed up to the equilibrium temperature (Figure 2 (a); points 3-4) (Borde, 2010).

The evaporation rate of the drying process can be described as (Jaskulski et al., 2018):+

$$-\frac{\mathrm{d}m_p}{\mathrm{d}t} = f A_p \beta_p (C_{sur} - C_{amb}) M_p \tag{21}$$

where M_p is the molar mass of the particle, C_{sur} and C_{amb} represent the molar concentration of vapours evaporating on the particle surface and on the ambient air, respectively. The mass transfer coefficient is represented by β_p and can be determined using Ranz-Marshall correlation (Woo, 2016):

$$\beta_p = \frac{D_{vap}}{d_p}\left(2.0 + 0.6\mathrm{Re}_p^{\frac{1}{2}}\mathrm{Sc}^{\frac{1}{3}}\right) \tag{22}$$

where D_{vap} is the diffusion coefficient of vapor and Sc is the Schmidt number (Jin & Chen, 2009).

The molar concentration can be determined as (Jaskulski et al., 2018):

$$C_{sur} = \frac{p_{sat}}{RT_P} \qquad C_{amb} = y\frac{p_{op}}{RT_{amb}} \tag{23}$$

where p_{sat} and p_{op} represents the partial pressure of saturation and operation, respectively, R is the universal gas constant and y the species mass fraction in vapour.

The evaporation rate, Equation (21), also includes a relative drying rate coefficient f that is responsible for describing the different stages on the drying process. For the first drying stage (Woo et al., 2008):

$$f = 1, \qquad \text{if} \quad X > X_{cr} \tag{24}$$

and, consequently, evaporation rate follows Equation (21).

For the second drying stage (Woo et al., 2008):

$$f = \left(\frac{X - X_{eq}}{X_{cr} - X_{eq}}\right)^{n}, \qquad \text{if} \quad X < X_{cr} \tag{25}$$

Therefore, this stage can be nonlinear and characterized by polynomial functions. The exponent n can be determined experimentally. For maltodextrin DE12, n = 3.22 (Woo et al., 2008).

In the model, the value of critical moisture content was set as X_{cr} = 0.61 (Jaskulski, 2015).

This model will be incorporated in UDF code to describe multicomponent droplet evaporation (Appendix A).

2.2.4 Droplet coalescence and particle agglomeration

When atomization is turned on, there is an intense mixing between spray and hot air, which leads to droplet and particle collisions. This phenomenon has a significant impact on dehydration rate and on the product size.

There are three types of collisions: collision among two droplets, droplet-particle collision and collision between two particles (Ali et al., 2015).

Collisions between two droplets can result in the formation of a new droplet in a process called coalescence that happens mainly inside the atomization zone, that comprehends the angle region where nozzle is spraying, where $X > X_{cr}$. However, depending on the droplet velocity, two additional scenarios can occur: if the velocity is too high, as a result of the impact, droplets may be fragmented into smaller fractions; otherwise, if the velocity is not high enough to break the surface tension, the droplets simply collide, without coalescence (Jaskulski et al., 2018).

Particle-liquid droplet collisions are possible in cases where dry particles are recycled back into the atomisation zone. In this case they merge and dry particles become covered with solution from the liquid droplet (Jaskulski et al., 2018).

When two particles collide, depending on their moisture content and temperature, they can agglomerate to form a bond. Electrostatic and van der Waals forces can be established between the particles, forming an agglomerate. However, these bonds are not stable and will not last, undoing the agglomeration. Therefore, will not affect the size distribution of the product. Agglomeration is achieved as a final product when a liquid bridge that is strong enough to resist mechanical deformations is formed (Verdurmen et al., 2006). Due to continuous drying, the bridge solidifies, and a new particle is formed, with larger dimensions and irregular shapes (Jaskulski et al., 2018).

Agglomeration can also happen due to stickiness. Stickiness is a physical change on the surface of the particle, that is strongly influenced by particles moisture content, surface temperature and material properties. This phenomenon can be seen as one of the biggest problems in the spray dryer processes. Stickiness can lead to agglomeration, changes in bulk density, shape and size of the final product, causing wall deposition of materials, frequently cleaning and excessive plant shutdowns. It is not only a matter of product quality, but these consequences will have repercussions on storing and packaging of the product, raising costs. However, there are some industrial facilities in which stickiness is used as a method for production of granulate powders as a final product (Adhikari et al., 2005; Gianfrancesco et al., 2010).

Most of the computational methods found in the literature to determine stickiness are based on the glass transition temperature (T_g) of the material (Woo, 2016). Hereupon, analysing changes in the T_g makes it possible to determine the agglomeration zones inside the drying chamber. Predicting particle stickiness could help in reducing operational issues (e.g., dryer fouling) or performing agglomeration to adjust final powder qualities (Gianfrancesco et al., 2010). An illustration of agglomeration and coalescence phenomena can be seen in Figure 1.

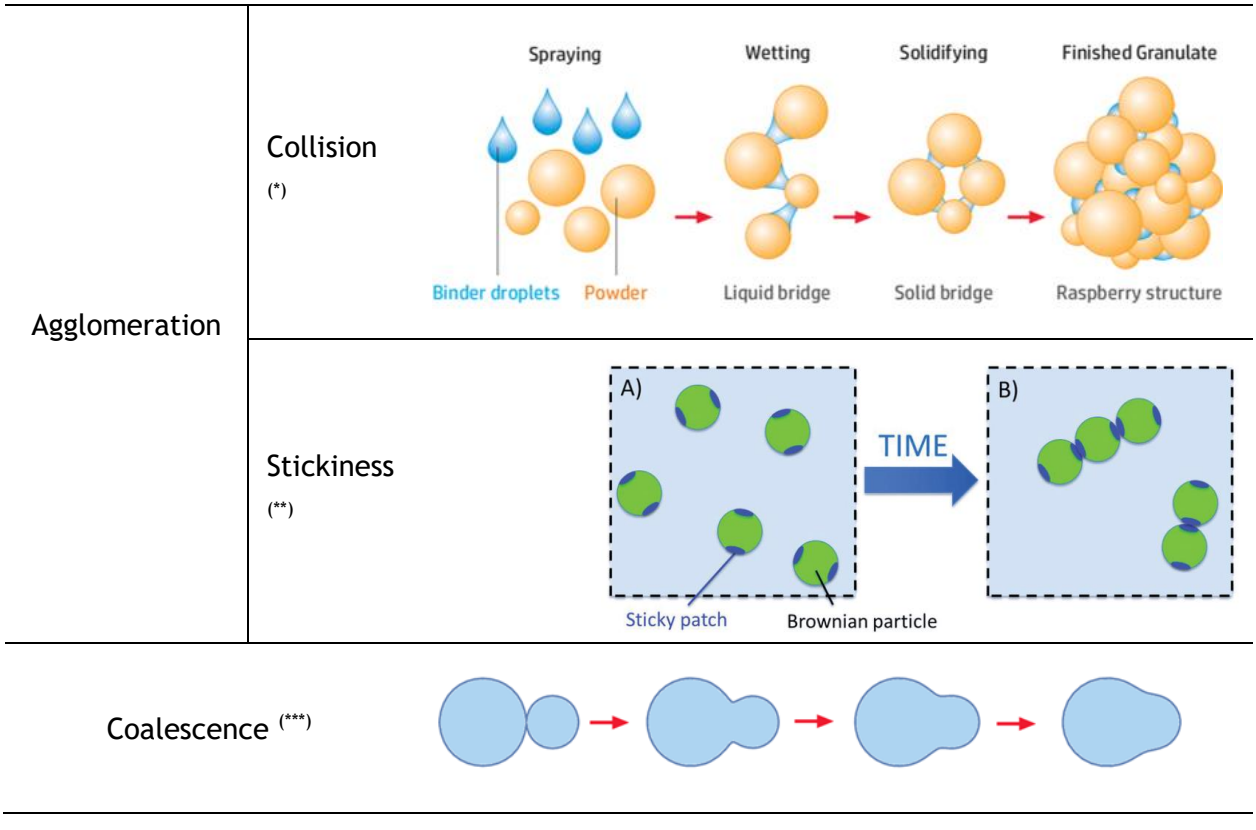

Figure 3 Agglomeration and coalescence phenomena.

(*) Source: (IPC Dresden, n.d.)

(**) Source: (Hong et al., 2016)

(***) Source: (Dahiya et al., 2016)

2.2.5 Modelling stickiness of particles

Currently, there are no models in Ansys Fluent that can be applied into DPM models that would allow to predict the structure of the resulting agglomerates (Verdurmen et al. 2004). This phenomenon is extremely difficult to predict due to the way particles are described in the software. Particles are presented as material points with zero-volume, which makes it impossible to simulate collisions between droplets and particles. Other approaches have been adopted to map the agglomeration process, one of which is related with the glass transition temperature.

The glass transition temperature is a specific property of amorphous materials. Above this temperature, the material experiences a transition from rigid to a more flexible state caused by the adjustments in the material structure (Adhikari et al., 2005). This temperature can be used as an indicator of surface stickiness. When a particle is heated above its T_g the surface becomes sticky, causing adhesion between particles or the surface of the equipment. The temperature above T_g to which a particle starts to be sticky is called sticky point temperature and it depends on material and on moisture content (Gianfrancesco et al., 2010). For the present study, a particle is considered to agglomerate when $X < X_{cr}$.

According to Gianfrancesco et al. (2010), the particles surface can be considered sticky when the temperature of the particle is higher in a range of 10 ºC to 30 ºC than the T_g. *H*owever, if the temperature is raised too much, particles lose their stickiness and begin to ignite.

The sticky temperature concept can be better understood observing Figure 4.

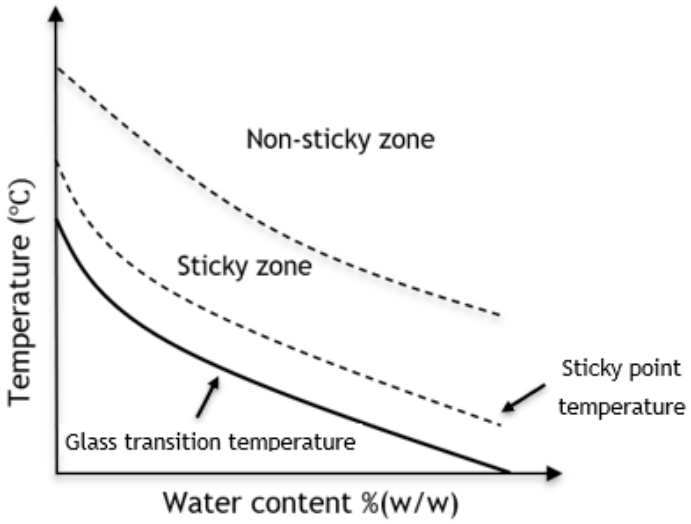

Figure 4 Glass transition and sticky temperature.

Agglomeration can be avoided if the operating temperatures are kept below T_g. Another alternative would be using a co-current geometry, since both phases in parallel minimize mixing of phases and hence the probability of particles to collide and agglomerate (Jaskulski, 2015).

The Couchman-Karasz relation describes the effect of moisture content on the T_g, and it is expressed by Equation (26), for a mixture of two components (Siemons et al., 2020):

$$T_g = \frac{y_s \Delta c_{P,s} T_{g,s} + y_w \Delta c_{P,w} T_{g,w}}{y_s \Delta c_{P,s} + y_w \Delta c_{P,w}} \quad (26)$$

where y_s and y_w represent the weight fractions, $T_{g,s}$ and $T_{g,w}$, the glass transition temperature, and $\Delta c_{P,s}$ and $\Delta c_{P,w}$represent the heat capacity change at glass transition temperature of the solute and of the water, respectively.

This equation can be rewritten into Equation (27) assuming $k_1 = \Delta c_{P,s} / \Delta c_{P,w}$, which is often referred to as Gordon-Taylor equation (Siccama et al., 2021):

$$T_g = \frac{k_1 y_s T_{g,s} + y_w T_{g,w}}{k_1 y_s + y_w} \quad (27)$$

Gordon-Taylor equation has been shown to be adequate to estimate the T_g of many materials. This equation is a function between T_g and the moisture content of the droplet, where T_g decreases as the moisture content increases (Ozmen & Langrish, 2002). Therefore, in order to use this equation for the prediction of stickiness, it is required the knowledge of the drying kinetics of droplets, which will be obtained with the data collected from the CDC model.

For an aqueous solution of maltodextrin DE12, different values of $T_{g,s}$ were found on the literature (Frías et al., 2001; Siccama et al., 2021). Ideally, the $T_{g,s}$ should be determined using Differential Scanning Calorimeter (DSC). To determine $\Delta c_{P,s}$, the sample should be heated, and from the resulting thermograms this parameter could be determined (Pycia et al., 2016). Since these measurements were not possible, values from literature were used. The $T_{g,s}$ *for* maltodextrin DE12 was 426 K and the $T_{g,w}$ for water was 139 K. A value of 0.426 kJ kg^{-1} K^{-1} was used for the heat capacity of maltodextrin ($\Delta c_{P,s}$) and 1.91 kJ kg^{-1} K^{-1} for water ($\Delta c_{P,w}$) (Siccama et al., 2021; Siemons et al., 2020).

Since the sticky temperatures are unknown, some tests with distinct differences between the actual particle temperature and glass transition temperatures $(T_p - T_g)$ will be performed, in order to find the agglomeration zones. In this study, three sticky conditions were considered:

- Case I: $\Delta T = (T_p - T_g) > 5$ °C
- Case II: $\Delta T = (T_p - T_g) > 10$ °C
- Case III: $\Delta T = (T_p - T_g) > 15$ °C

Stickiness is especially important in the production of sugars due to its inherent stickiness. When the sticky point is reached, particles adhere to each other. Then, a liquid bridge between the particles is formed from the melting of sugars that caramelize and are converted into solid

bridges (Hashemi et al., 2017). These differences between T_p and T_g means how fast the sugar is melting and since this border is unknown, different values are established to determine which difference is more reasonable.

Gordon-Taylor equation will be implemented on the code using an UDF to calculate $T_g$as a function of moisture content of the particles (Appendix A). Then, the T_g will be compared with the actual temperature of the particles, and the conditions for agglomeration will be set as 0 if agglomeration does not occur, or 1 if agglomeration occurs. DPM model allows to track the position of particles and thus determine possible agglomeration zones by stickiness.

From Section 2.2.4 it is known that particles do not necessarily coalesce or agglomerate when humidity and temperature conditions are favourable. This phenomenon also depends on the impact angle and momentum of the particles. However, for this study these parameters are not considered. In counter-current systems the impacts are rather fast due to the intense mixing of the particles. Therefore, it is very likely that most of the particles will collide. For co-current systems, where particle velocities are much lower, these parameters are normally observed. It is important to emphasize that the simulations are an approximation on reality.

After determining the agglomeration zones, these results must be validated with experimental data.

3 Materials and Methods

The CFD experiments are based on a pilot-plant counter-current spray dryer powered by two-nozzles, located at Lodz University of Technology at Faculty of Process and Environmental Engineering in Poland.

3.1 Counter-current spray dryer installation

The counter-current spray-drying tower shown in Figure 5 was the subject of the simulations.

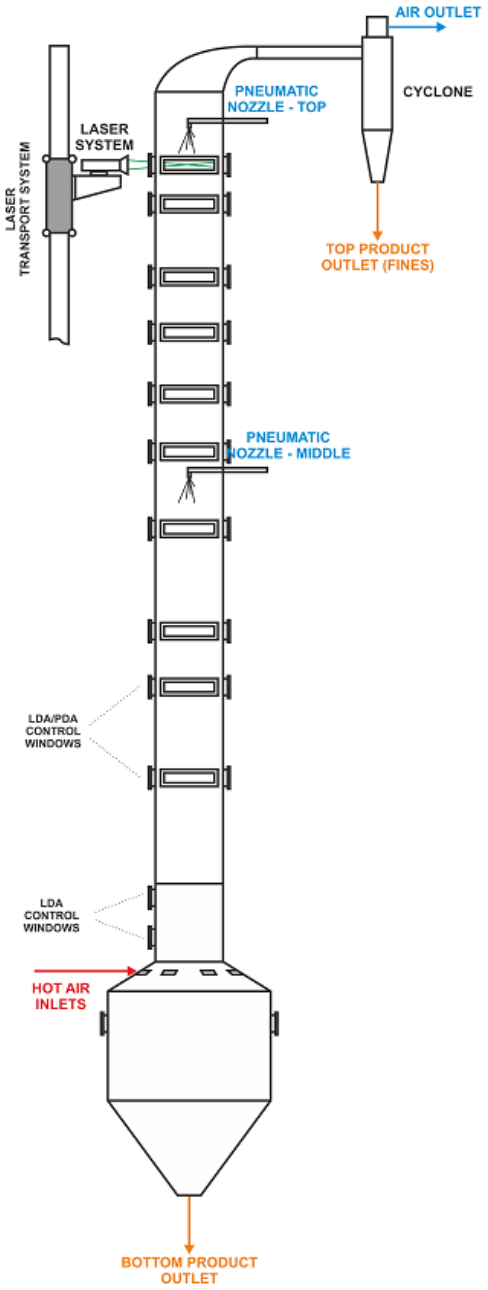

Figure 5 Counter-current spray drying installation.

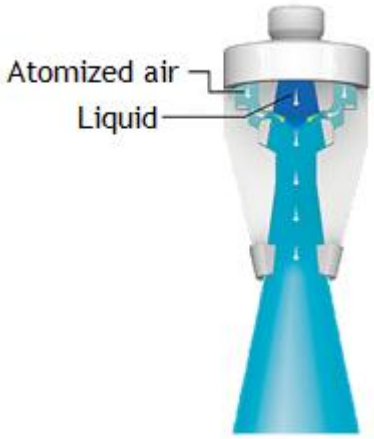

Figure 6 Twin-fluid nozzle with internal mixing (Lechler, 2022).

The experimental installation is a column with 0.5 m diameter and 7.4 m height. Since it works in counter-current mode, the inlet of drying air is located at the bottom of the column, at a distance of 1.3 m from the column base, and the inlet of slurry is made from the top, using nozzles. This column is equipped with two nozzles, one at 7.2 m and the other at 3.8 m from the bottom, each one spraying 4 $kg\,h^{-1}$ of slurry. The contact of phases occurs in the tower, after the hot air flows from the distribution ring to the drying chamber through 8 perpendicular connection ducts.

First, the slurry is prepared in a tank, located at the bottom of the installation, where steam is used to increase the temperature of the raw material. Then, slurry is pumped until it reaches the middle and the top of the column, where a thermostat and a flow meter are used to control the inlet temperature and measure the flow rate, respectively. The solution is then fed to the tower through the nozzles, displaced at different heights, that disperse the liquid stream in a mist of fine droplets. At the same time, a hot air stream enters tangentially at the bottom of the column through the 8 connection ducts. The final product, dry powder, is recovered at the bottom of the dryer.

An air purification system is used to collect powder remnants on the outlet of air. Air first goes through cyclones, then passes through a bag filter that is followed by an air-cooling system and again through another bag filter. Finally, air goes through an exhausting dedusting system before being released into the environment. The leftovers collected are then sent to an appropriate treatment facility.

In order to reduce heat losses, the drying chamber was insulated with 4 cm layer of glass wool.

Two laser devices, LDA (Laser Doppler Anemometry) and PDA (Phase Doppler Anemometry) move along the drying tower to measure the velocities, diameters and direction of droplets/particles.

The nozzle used is a pneumatic nozzle, more specifically, a twin-fluid nozzle with internal mixing (Figure 6). This type of atomizer uses two fluids: gas, usually air, and liquid, which is the substance to be powdered. Initially both fluids are separated in the atomizer. Then, fluids are mixed inside the nozzle chamber and the gas forms bubbles. When exiting the nozzle, the compressed mixture expands the spray, producing very fine droplets (Lechler, 2022). Depending on the atomizer and solution used, droplet size will be different.

For this work, 40 % (w/w) solution of maltodextrin of Dextrose Equivalent 12 (DE12) in water was used as a raw material. In addition to being a low-cost reagent and easy to find on the market, it is also easy to clean and non-hazardous, making it simple to handle. Maltodextrin DE12 has a density of 1568.2 $kg\,m^{-3}$ and a specific heat of 2464 $J\,kg^{-1}\,K^{-1}$ (properties provided by the supplier).

3.2 Computational mesh generation

The geometry of counter-current spray dryer was constructed on AutcoCAD software by a laboratory associate and is reproduced in Figure 7.

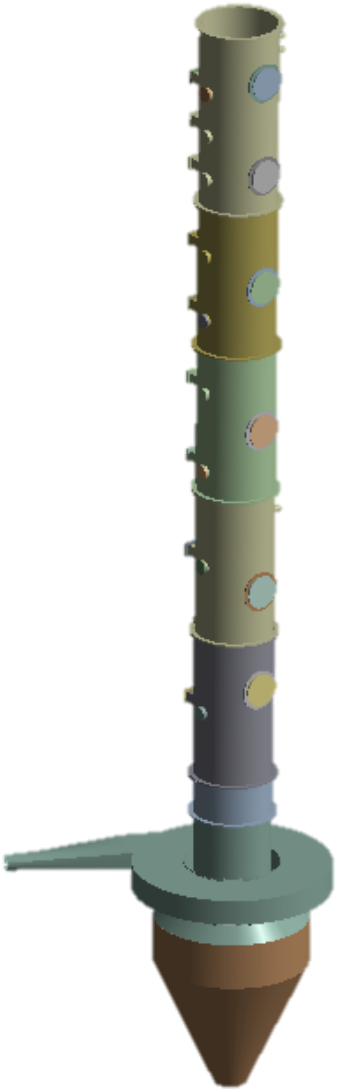

Figure 7 Counter-current spray dryer geometry.

With the purpose of efficiently construct the 3D CFD model of the process, the modelled geometry was simplified. Specifically, the maintenance holes and the control windows of the tower were removed.

For the geometry represented in Figure 7, the calculation time lasted several days. Therefore, it was necessary to reduce the number of elements of the generated computational mesh and thus the simulation time. For that purpose, the spray dryer geometry was divided into two parts: distribution ring and drying chamber.

CFD simulation is based in numerical methods applied in geometry volumes. Inside the drying chamber, the continuous phase fills the entire volume. In order to be possible to perform calculations, this volume must be divided into smaller elements. This is known as discretization process, and it results in the creation of a computational mesh, which constitutes the computational domain.

In the next sub-chapter, the mesh of distribution ring and drying chamber are displayed. Simulations will be performed on Ansys Fluent program (version 2022 R1).

3.2.1 Distribution ring

The distribution ring was simulated using simply the continuous phase. The first mesh was obtained adopting Cartesian model which contained 380k quadrilateral elements. This mesh had an acceptable skewness (about 0.97). Analysis of the temperature contours in cross section of the ring revels negative values, demonstrating that this mesh was not able to provide a physically realistic and convergent solution. As a result, the quadrilateral mesh was replaced with a tetrahedral mesh containing hexagonal elements, which exhibits better quality.

To improve the quality near the walls, inflation layer control was added. Normal to the wall, velocity and temperature gradients are much higher than gradients parallel to the wall. Inflation layer creates thin elements that can capture the normal gradient with minimal elements (Simutech Group, 2022). To take more advantage of inflation, a specific layer was created in each body part of geometry using the thickness of the first boundary layer (y_H) and the number of boundary layers (N) determined for each body. These values can be determined applying equations (A.1) to (A.10) presented in Annex A.

The first tetrahedral mesh contained 480k hexagonal elements and a maximum skewness of 0.97. Some refinements were progressively made increasing the number of elements of the mesh. In general, the finer the discretization, i.e., the smaller the element size is, the more accurate the simulation. Nonetheless, a mesh that is too fine will consume a lot of computing power, increasing the simulation time. One strategy for starting the simulation is to choose a mesh size that is able to give realistic results, and then gradually refine the mesh (Woo, 2016).

Meshes with 380k, 450k, 480k, 500k and 570k number of elements were generated. An independency mesh test was made, and results showed that meshes with more than 480k elements do not improve the results, just increase the computational power.

Finally, a mesh containing 482k hexagonal elements was selected, which is represented in Figure 8 in two different views.

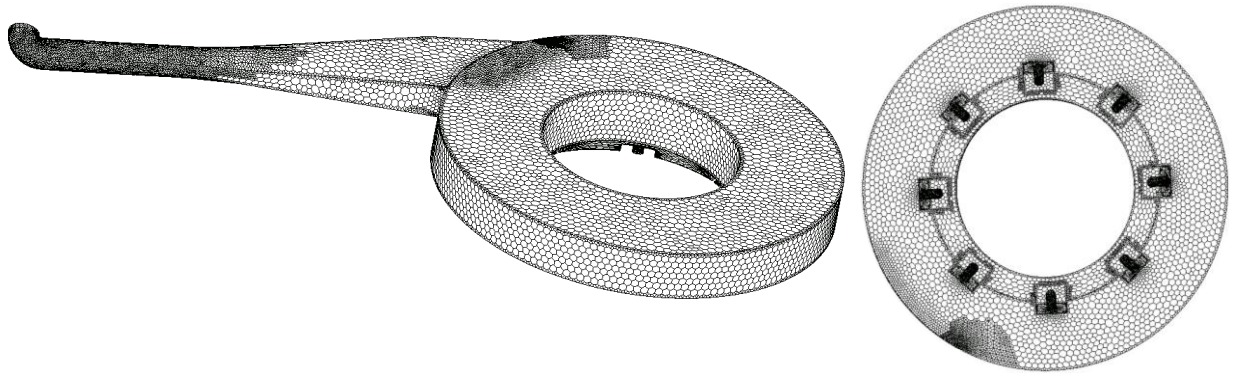

(a) (b)

Figure 8 Computational mesh of the distribution ring generated with 482k elements: (a) Top view; (b) Bottom view.

To validate the mesh, the results obtained from simulation were compared with experimental ones, for the same conditions. A thermocouple was placed inside one of the connection ducts and the temperature was measured for different inlet conditions.

Simulated and measured temperatures, for the same connection duct, were compared. The analysis of the temperatures shows that the tetrahedral mesh with 482k elements provides similar results when comparing with the measured values, validating the mesh created and the numerical method. These results can be presented in Table B- 1, Appendix B.

3.2.2 Drying chamber

Following the same procedure as described in the previous section, the mesh of the drying chamber, schematized in Figure 9 (a), was also created. Two different meshes were generated: one block-structured mesh with 808k elements and skewness equal to 0.99 (Figure 9 b) and one non-structured tetrahedral mesh with 1210k elements and with skewness equal to 0.96. Tetrahedral mesh displays better quality and was selected to compute the simulations.

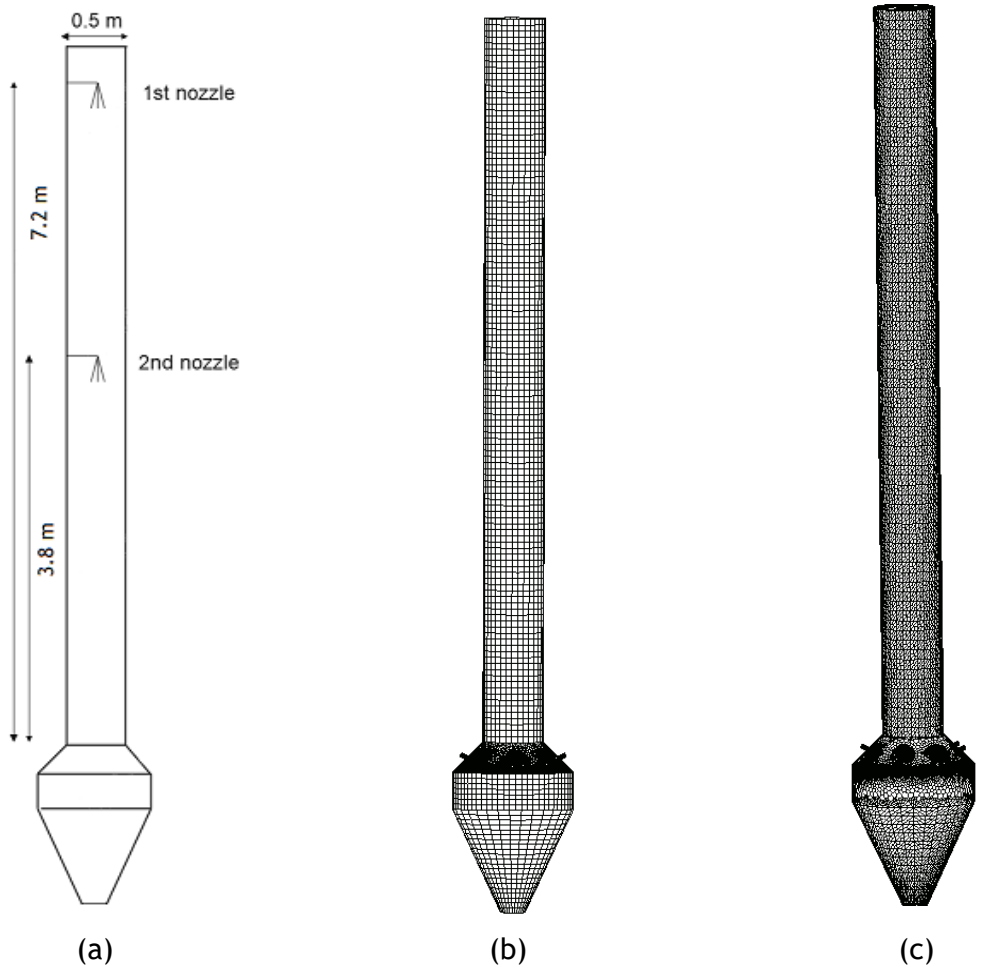

Figure 9 Schematic drawing of dryer chamber geometry (a) and two generated computational meshes: (b) block-structured mesh (808k); (c) non-structured tetrahedral mesh (1500k).

Various tetrahedral meshes with different element sizes were generated. Meshes with 1210k, 1420k, 1500k, 1690k, 1810k and 1890k number of elements were created.

A mesh independency test was performed in order to find a mesh whose results are independent of the number of cells used in the computational domain. Results show that the mesh with 1500k elements (Figure 9 c) has the best performance and that using denser computational meshes does not affect significantly the accuracy of calculations, just increasing the calculation times.

3.3 Boundary conditions

Most of the boundary conditions were based on experimental conditions of the spray dryer. Once the spray dryer geometry was divided in two, the air mass flow rates and temperatures obtained in each connection duct in the distribution ring were used as boundary inlet conditions in the drying chamber. These values are presented in Table C- 1, Appendix C. However, the set point in the chamber for the inlet temperature was controlled only in one connection duct.

The outlet of the particles located at the bottom of the dryer, was defined as a wall, blocking the passage of air but being permeable to particles. The upper outlet of air was defined as a free flow.

For the gas phase inlet to the tower, the direction was stated as normal to the boundary.

The initial droplet size distribution is based on the Rosin-Ramnler method. The maximum, mean and minimum droplet size are 250 μm, 133 μm and 1×10^{-5} μm, respectively. It was assumed that droplets have an initial uniform velocity of $11.87\,m\,s^{-1}$. Due to technical problems with the laser measurement system, it was not possible to determine the Particle Size Distribution (PSD) of the particles or their velocity. These values are based on Jaskulski (2015), acquired for similar conditions for the same material.

On the walls, a no-slip boundary condition was set, which means that the fluid will have the same velocity as the boundary at a solid border, creating a significant velocity gradient in the wall normal direction. The reflecting particles on the wall were also set as a boundary condition.

In the simulation, the outlet of the air was simplified. In the real equipment, the outlet is followed by a cup and a pipe that conduces the air into the cyclones. The air temperature in the cup is high, corresponding to the air temperature that is leaving the tower. This simplification causes some problems in the simulation of the flow behaviour near the outlet, creating a reverse flow that enters the tower. It is difficult to impose the exact conditions in case a reverse flow happens, and some errors can appear in such region. However, the simulation must consider the average temperature of air that could be entering the tower. In this way, the exhaust air outlet was set with a backflow temperature based on the experimental outlet temperatures.

Other parameters at the boundary are given in Table 1 for different essays.

Table 1 Boundary conditions.

		Essay A	Essay B	Essay C
Air inlet (distribution ring)	Total flow rate	160 $Nm^3 h^{-1}$	100 $Nm^3 h^{-1}$	160 $Nm^3 h^{-1}$
	Temperature	291.4 °C	321.0 °C	221.0 °C
Air inlet (tower)	Temperature	240.0 °C	240.0 °C	185.0 °C
Air exhaust	Pressure		1.013×10^5 Pa	
	Backflow Temperature	90.0 °C	65.0 °C	70.0 °C
Atomization	Temperature		80.0 °C	
	Mean droplet size		133 µm	
	Particle velocity		11.87 $m s^{-1}$	
	Cone spray angle		13 °	
	Slurry flow rate		4 $kg h^{-1}$	
	Air flow rate		8 $kg h^{-1}$	
Walls	No-slip			
	Reflecting particles			

3.4 Heat losses model

In order to study heat losses from the spray drying chamber to the environment, a single-phase CFD modelling was carried out for Essay A. Analysis of temperature distribution through the tower allowed to observe that the temperature field is not uniform, existing a temperature drop of 147°C, implying heat losses from the tower to the environment. The heat losses through the tower were already expected since experimental tests performed only with the continuous phase allowed to verify a temperature drop between 145 - 172 °C from the inlet to the outlet.

These losses will affect the temperature distribution during the process and, consequently, the drying rate. Therefore, to accurately describe the drying process and agglomeration, a heat losses model was implemented in CFD simulation.

Employing a heat losses model in a spray dryer can be challenging. In general, the geometry of the equipment is complex. Considering that the maintenance holes and the control windows are not insulated, as well as the ribs on the flanges, becomes even harder to determine a local heat losses coefficient.

One approach to determine the heat losses is to approximate an overall convective heat transfer coefficient for the chamber. This approach has been tested for several pilot-scale spray dryers and provided reasonable results (Woo, 2016).

Therefore, an overall convective heat transfer coefficient (α_p) was determined for the geometry in study and implemented on Ansys Fluent to determine the heat flux to the environment. The overall coefficient was calculated resorting to total heat transfer equation, Equation (16), in conjunction with convective heat transfer equation, Equation (17). The determined value of α_p was 3.43 $W m^{-2} K^{-1}$ for essay A.

In order to create a heat flux expression, Equation (17) was slightly rearranged, dividing both members by the heat transfer area. This expression was defined in Ansys Fluent, using the determined overall coefficient and a temperature difference between the walls of the tower and the exterior. The temperature in the walls was defined as wall adjacent temperature to capture the profile near the walls. The ambient temperature was considered constant and equal to 20°C. The wall in direct contact with the distribution ring was considered adiabatic.

Figure 10 presents the heat flux contour through the insulated column wall to the surroundings, after applying the heat losses model. The negative sign in heat flux values indicates that the heat is dissipated from the tower to the exterior.

The maximum values of heat flux are achieved at the bottom of the chamber with 691 $W m^{-2}$, due to the hot air supplying from the distribution ring in this section. As the gas loses energy through the tower, temperature gradient between the dryer and the environment decreases as well as the heat flux. The average heat flux taken from simulation for this essay is 440 $W m^{-2}$. The average heat flux predicted by calculations through the column walls is 532.2 $W m^{-2}$. The simplification done when adopting and overall heat losses coefficient will generate differences on local temperatures between CFD simulation, measured and theoretical values. However, on the overall conditions this impact will not be significant. Therefore, the comparison between heat fluxes shows good agreement between experimental and calculated results.

Table C-2 in Appendix C lists the values for the calculated heat transfer coefficient (α_p), theoretical heat flux, and obtained by CFD simulation for different essays.

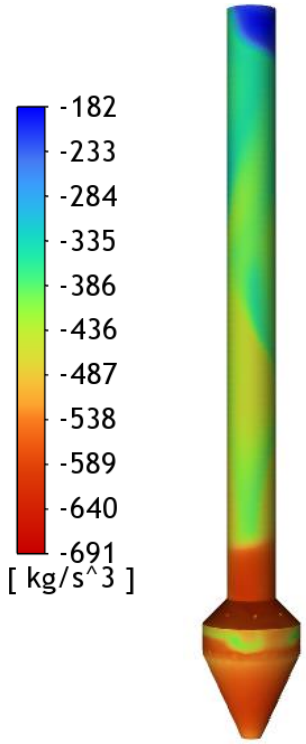

Figure 10 Heat flux profile [kg s^{-3}] for the continuous phase when applied heat losses model in the drying chamber.

3.5 CFD simulation Initialization

In the drying chamber both continuous and discrete phases coexist. The trajectory of the discrete phase is influenced by the prediction of air velocity profiles of continuous phase inside the tower. Therefore, prior simulation of the continuous phase is required.

As a first step, only the continuous phase was modelled inside the dryer chamber. It was necessary to define whether the calculations would be performed in steady or transient state. First, the steady state was analysed since most of the spray dryers found in the literature perform simulations under steady state conditions (Razmi et al., 2021). However, a convergent solution was not achieved due to the instability of airflow inside the chamber, and a transient regime was adopted. A transient flow is more stringent in terms of required computational resources and computational time due to time dependency.

For calculations in transient state, the time step size (Δt) and the number of time steps for the simulation to run must be chosen. The time step size must be such that fluid and particles move at most one mesh element in each time step (i.e. Co < 1, where Co is the Courant number). Additionally, the time step must be small enough to resolve time-dependent features and maintain solver stability (Ansys FLUENT, 2020).

A time step size of 0.2 s was chosen. The solver ran for 500 time-steps, each one with 27 iterations, which was sufficient to fully develop the flow field.

The number of iterations per time step was selected considering the number of DPM time steps. The DPM injection should not coincide with the continuous phase injection in order to avoid instabilities.

Before starting the calculations, it is necessary to set the boundary conditions, select the turbulence model, include the heat losses model and the DPM injection from both nozzles. If the calculations do not achieve the convergence criteria, other turbulence models should be tested. If this approach is not sufficient, the mesh should be improved. The $k-\varepsilon$ model was used to predict the turbulent flow of the gas phase.

4 Results and discussion

4.1 CFD simulation of the distribution ring

In the distribution ring, due to the stable airflow, simulations were run in steady state conditions. The profiles were generated for the inlet conditions of essay A.

In order to analyse the behaviour of the continuous phase flow inside the distribution ring, contours of pressure, velocity and temperature were obtained from CFD simulations. Figure 11 shows the static pressure distribution in a horizontal cross section of the ring. The simulation results reveal a decrease in pressure at the entrance of the fluid to the ring, due to the frictional resistance of the walls and the higher velocity gradients. However, inside the ring, the pressure is more uniform, which indicates that the connection ducts to the tower all offer the same resistance and thus similar flow rates. The air flow pattern inside the distribution ring was similar for all the simulated cases.

To make the profiles more easy to visualize, a logarithmic scale was adopted.

Figure 11 Contours of static pressure [Pa] inside the distribution ring for essay A.

The velocity profile inside the distribution ring was also studied, as shown in Figure 12. According to the numerical results, the distribution of the air velocity is highly uneven, and decreases along the ring due to the increase in the flow area. It is clear that the air flows first near the walls, then toward the centre. The shape of the connective ducts to the tower may be seen in the centre, where the speed is lower. Near the inlet to the ring there is a fluid stagnation zone. An identicall flow field was obtained for other essays.

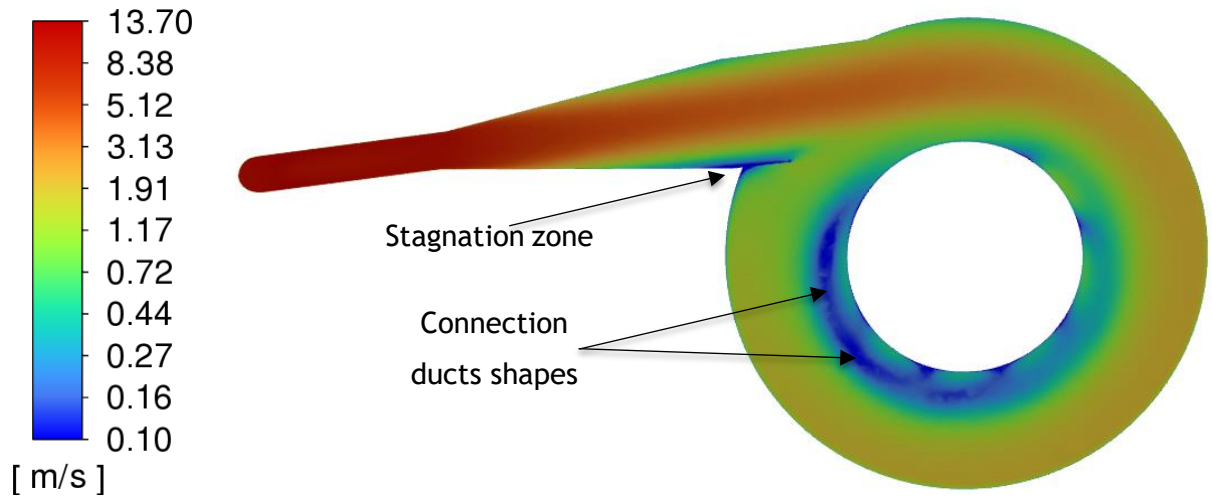

Figure 12 Air velocity field [m s^{-1}] inside the distribution ring for essay A.

The temperature distribution obtained using the energy balance can be seen in Figure 13. The numerical results show a non-uniform temperature distribution due to heat losses to the atmosphere. These results are consistent with experimental measurements since heat losses were already expected because the ring is not covered with any insulation layer. The average air temperature decreased about 70 °C from the entrance of the distribution ring until the connection ducts. The heat losses to the environment were estimated in 1322.2 W m^{-2} for essay A, 1244.7 W m^{-2} for essay B and 857.81 W m^{-2} for essay C.

Temperature fields obtained inside the connection ducts show good agreement with experimental values, and can be seen in the Table B- 1, presented in Appendix B.

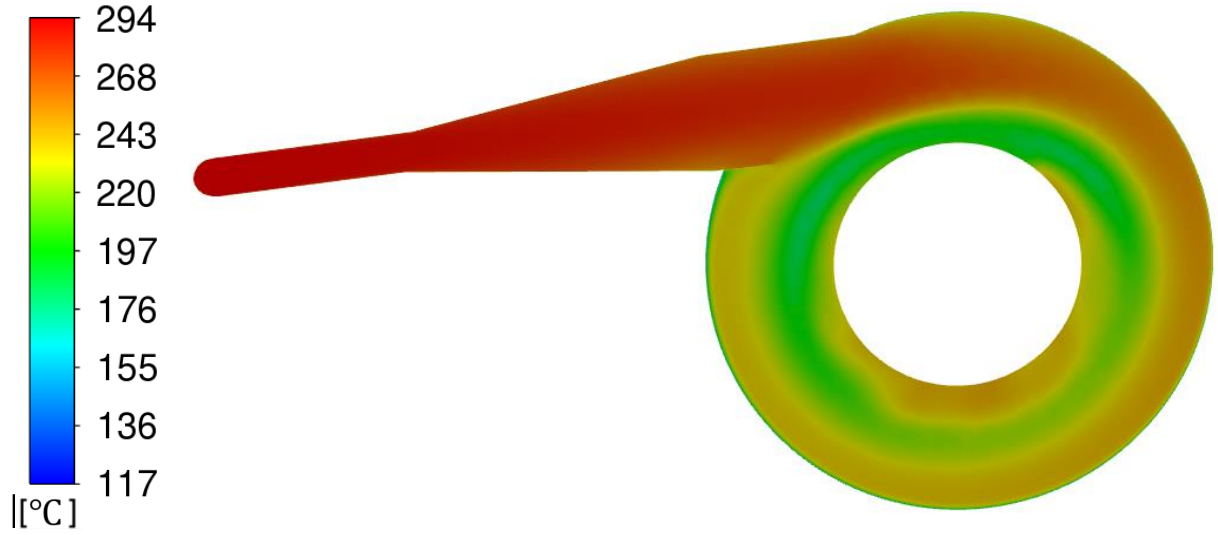

Figure 13 Air temperature distribution [°C] inside the ring for essay A.

Since the temperatures inside each connecting duct obtained in the simulation are different, they will be used as boundary inlet conditions at the drying tower in the following CFD simulations. Additionally, it was confirmed that the feed flowrate is distributed almost equally between the connection ducts.

4.2 CFD simulation of the drying chamber

The first 50 time-steps of simulation have been performed for continuous phase only, using a time-step size equal to 0.2 s. In this way, the calculations reached the convergence level and assisted the transition for the multiphase simulation. The DPM model was turned on and the simulation run for about 100 s of flow time for further analysis.

Figure 14 shows air temperature and mass fraction of water distributions inside the drying chamber equipped with two nozzles for two different essays at 80 s of flow time. The gas temperature is higher at the bottom of the tower, which was expected due to the hot air inlet in this region. Along the tower a temperature reduction is experienced as the heat exchange between the two phases and due to heat losses to the environment. The higher temperatures at the top of the tower in essay A compared to essay B demonstrate that higher flow rates cause a higher flow movement. Additionally, higher flow rates carry more energy, resulting in higher temperatures in essay A.

Droplet injection points are visible for essay A due to the entry of slurry at a lower temperature containing a higher water fraction content. The maximum water fraction occurs inside the spray zone, while decreasing outside of this zone due to the evaporation from droplets and wet particles. In essay A the sudden decrease of water content in the spray zone region suggests a maximum evaporation due to the initial free moisture at the surface. After the evaporation of surface moisture, the particles cool down causing the temperature of the surrounding air to decrease. In essay B the decrease in moisture content from the upper nozzle is not as noticeable due to the lower temperatures which prevent the particles from reaching the wet bulb temperature and thus evaporation. The lowest values of moisture content are registered at the higher air temperatures region in the bottom of the tower, drying almost completely the particles. In contrary can be seen that lower temperatures result in less evaporation leading to a higher water content on the particles. Between nozzles and below the lower nozzle, the gas temperature is more uniform and the changes in water content are small, indicating that the evaporation is low.

In essay B a dramatically decrease in water content is observed at the top of the tower. This change in moisture content is related to the reverse flow referred in section 3.3 and reaches low values once it is considered that the reverse flow air is completely dry.

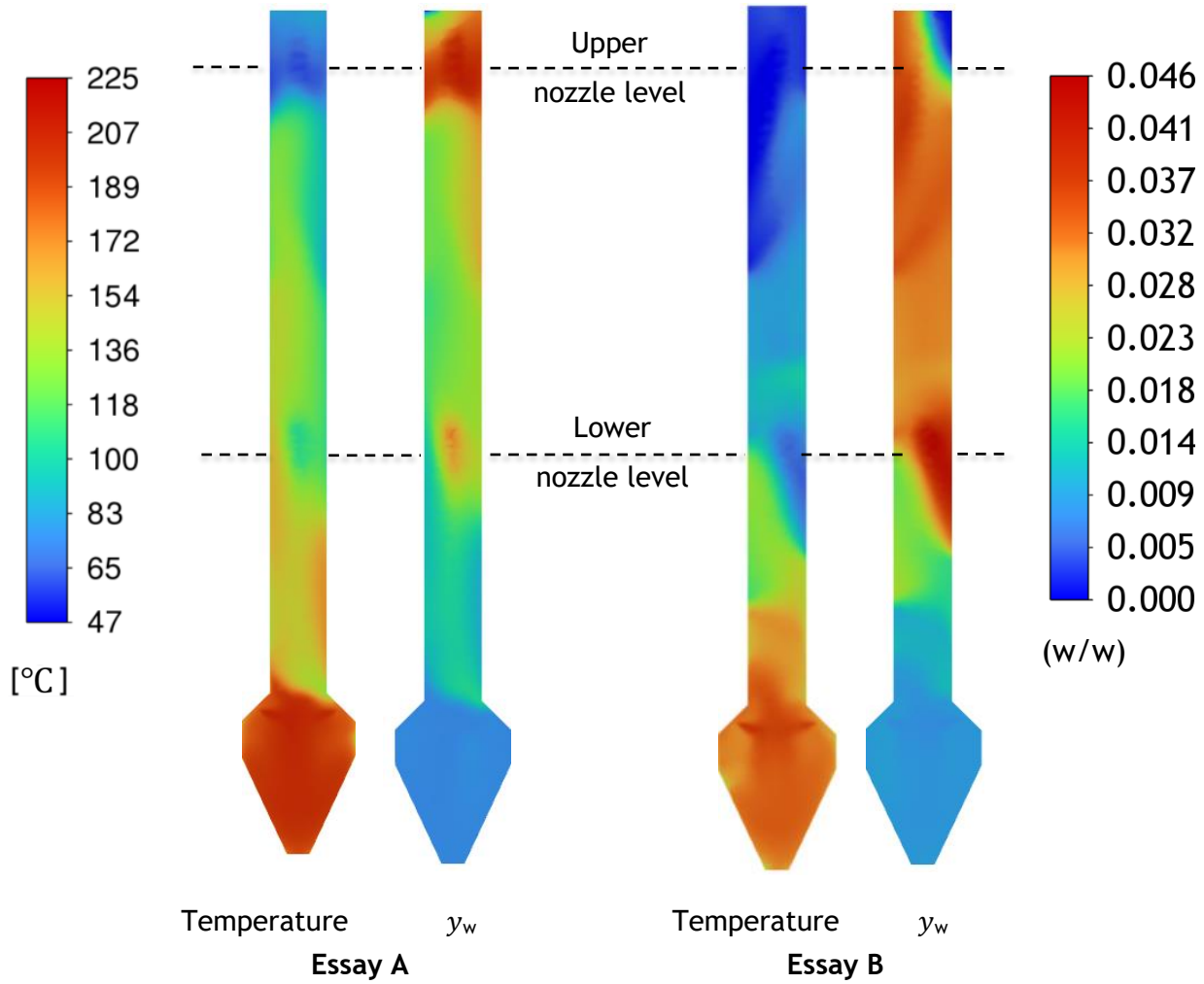

Figure 14 Air temperature [°C] and mass fraction of water (y_w) (w/w) distribution in an axial cross-section of the drying chamber.

Figure 15 shows the changes in airflow temperature at selected times inside the drying chamber for three different essays. It is possible to observe large changes in the temperature field over time. Note that the temperature field is asymmetric along the tower and that the flow is rotating, moving only from one side passing to the other. This behaviour proves that the flow is unstable.

Although the air in essay A carries more energy, the field in essay B initially reaches higher temperatures while maintaining similar but slightly lower temperatures along the tower compared to essay A.

Essay C has a lower initial temperature when compared to essay A and essay B. However, all essays reach identical temperatures throughout the tower due to the high heat losses to the environment. The flow field shows identical behaviour.

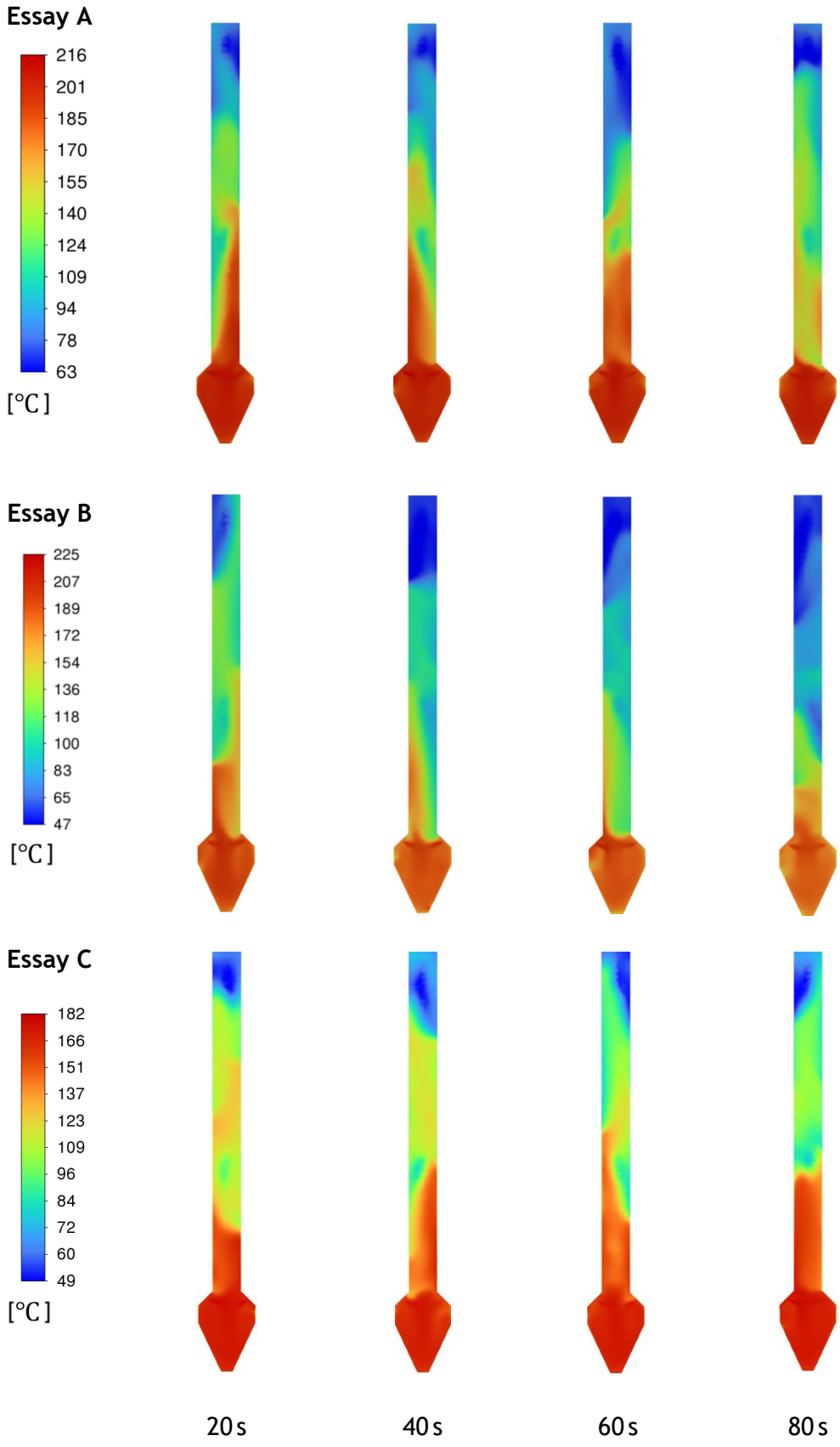

Figure 15 Air temperature [°C] field in an axial cross-section of the drying chamber for different times for essays A, B and C.

In the experimental tests, the measurements of the continuous phase along the tower are made at the operating windows located at different levels of the tower. Temperature readings were taken in each window at different distances from the centre of the tower.

Figure 16 plots the measured time-averaged temperature gas profile and the predicted gas temperature profile along the radial position at two different levels in the tower for Essay A. The experimental time-average measures were made by a laboratory associate that operates the spray dryer.

At the fourth window the temperature profile is parabolic, displaying the minimum towards the walls, peaking in the centre. However, for the window 9 located at the bottom of the tower, a flat profile is seen. As expected, temperatures decrease with greater distance from the bottom. Other profiles for different windows for Essay A and B are presented in Figures C- 1 and C- 2, Appendix C, respectively.

It is expected that the experimental results will vary from the simulation results. To perform the experimental measurements, a thermocouple is placed inside the chamber. During the measurements powder accumulates on the thermocouple, influencing the determination of the actual air temperature. Furthermore, the geometry has been simplified, as has the model implemented, which can lead to differences in temperature determination. Considering all the simplifications made, it is confirmed a satisfactory agreement by comparing the experimental results to those obtained by the simulation. Thus, the developed model correctly predicted air temperature inside the chamber, and so it is possible to ascertain that the particle temperature has been accurately determined.

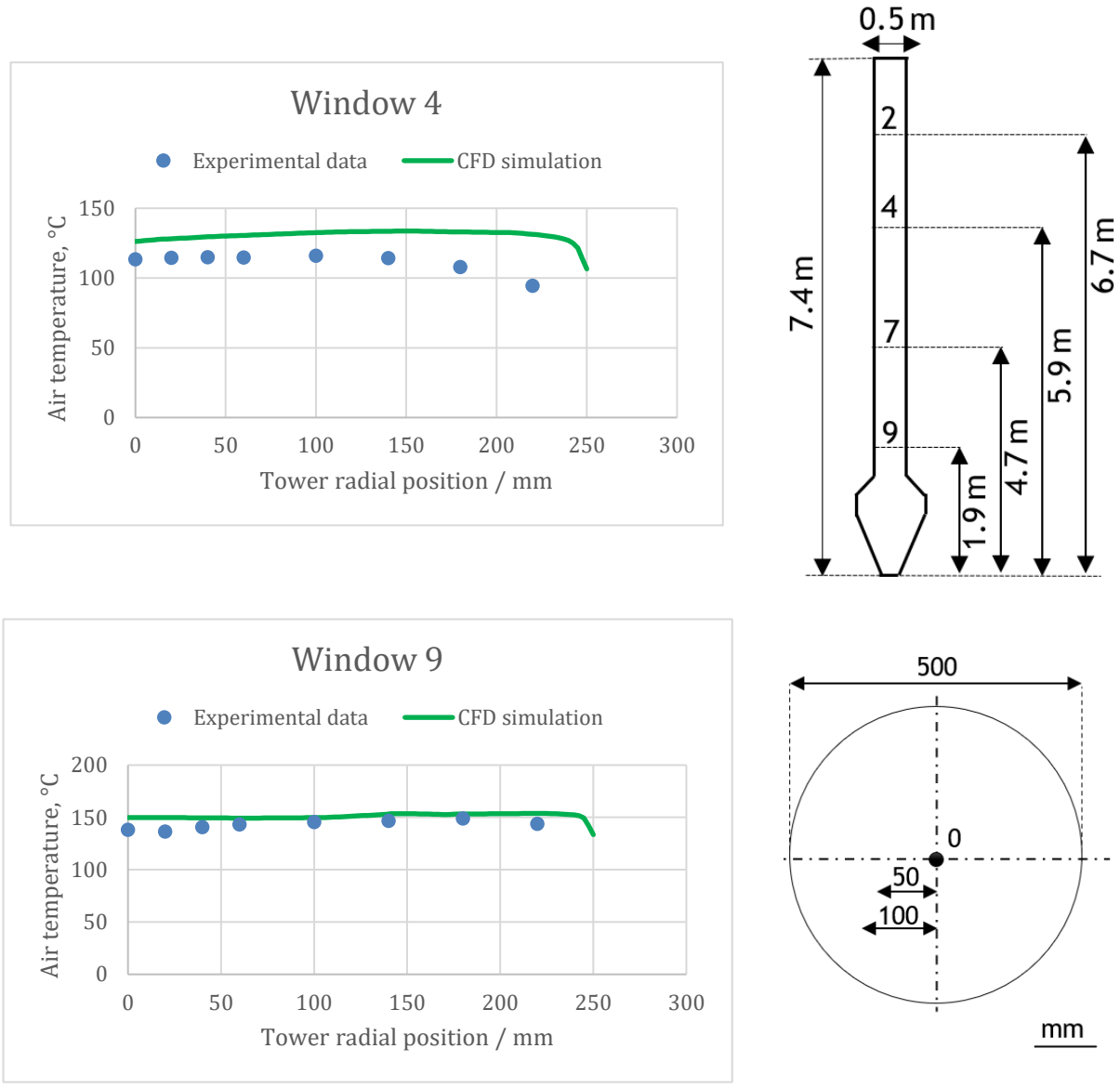

Figure 16 (a) Changes in mean air temperature [ºC] along the radial direction [mm] for different windows heights determined using CFD and obtained experimentally; (b) Spray dryer geometry with marked measurement window levels.

Figure 17 shows the axial air velocity distribution at different times. The velocity is maximum at the air inlets located at the bottom of the column. The air inlet in the tower has an angle of inclination which forces the air to move downwards. Once reached the bottom of the dryer the air flows along guided by the walls, reversing direction and rising in the dryer. Examining carefully the velocity fields, it can be observed that the air does not move uniformly along the column, but rather on one side and near the walls. During the flow of air through the tower, the flow can invert direction. Changes in velocity direction can be better observed in Figure C-3, Appendix C.

An analysis of the velocity field computed for essay B at 60 s allows to detect an unusual behaviour of the flow. Although the inlet is angled downwards, the air moves directly upwards. This phenomenon can occur due to the formation of a vortex in the inlet region which pushes the air against the wall causing it to change to an upward direction directly to the chamber. This condition is sporadic and for t = 80 s the flow returns to the downward direction. This situation demonstrates how the flow near the bottom is unstable.

A more stable profile was expected for the essay with lower flow rate, essay B. In contrary, opposing events are caused with an unstable flow due to the geometric configurations.

By superimposing the temperature and velocity fields, the areas of higher temperature match to those of higher velocity describing the path through which the fluid travels.

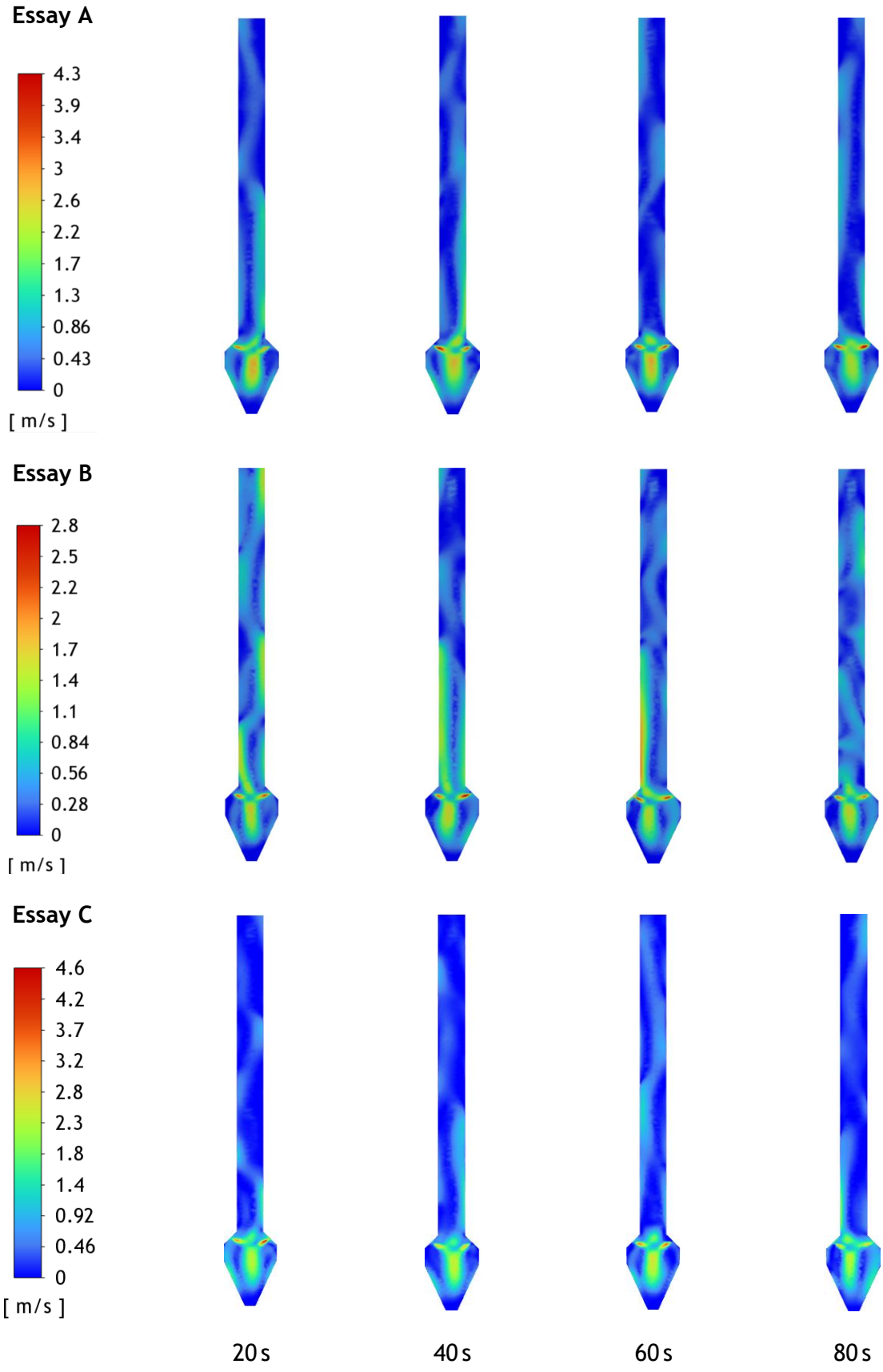

Figure 17 Air velocity fields [m s^{-1}] in axial cross-section of the drying chamber for different times for Essay A, B and C.

The predicted droplet/particle trajectories for each nozzle for essay A are represented in Figure 18, coloured by particle diameter. From the particle trajectories an intensive mixing of particles can be observed. Particle sizes range from 6.68 – 250 µm. The larger droplets/particles (250 µm) can be seen near the nozzles, while the average particles (125 µm) mostly reach the bottom leaving the dryer, but may also exit at the top, and the smaller particles (7.50 µm) are carried mainly to the upper air outlet.

Due to the intense mixing in the dryer, particles leaving the nozzle can have different trajectories. A fraction of particles travels near the walls reaching the cone at the bottom and returning to the tower. Other particles leave the nozzle and move directly to the outlet at the bottom or at the top. Particles from the lower nozzle can also directly move to the top. Some particles may not even come out of the dryer, remaining deposited on the walls or entering in a recirculating trajectory. Some examples of the stream's trajectories are present in Figure C- 4, Appendix C.

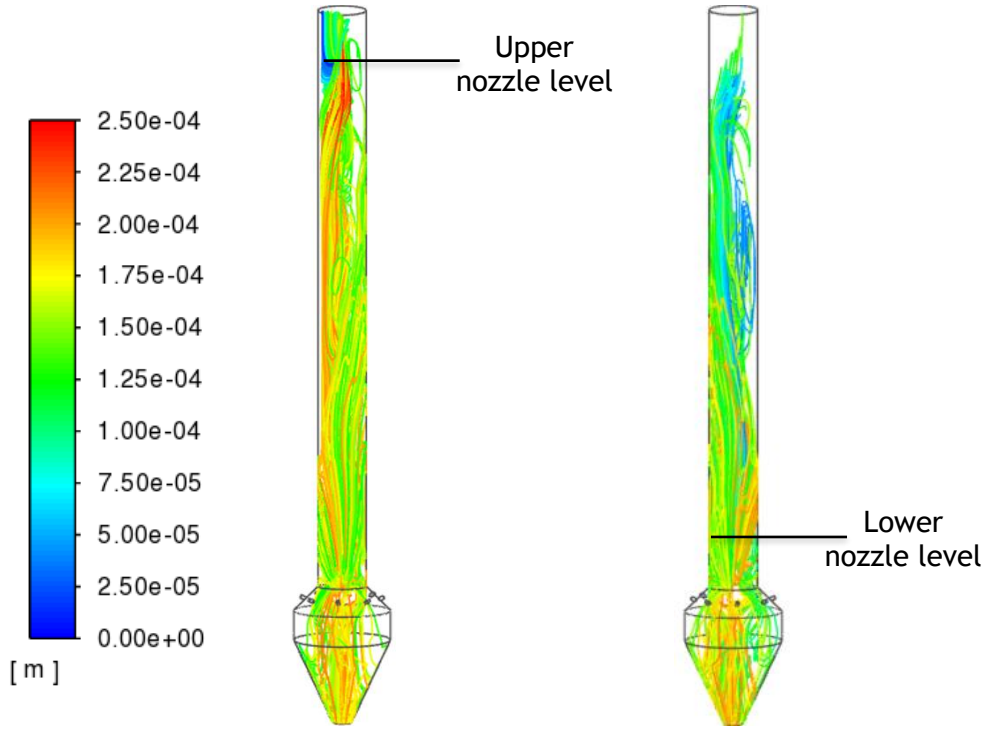

Figure 18 Particle trajectories from two nozzles: higher level nozzle on left and lower-level nozzle on right, coloured by particle diameter.

Distinct trajectories will lead to different particle residence times. For essay A, at the upper nozzle, the maximum particle residence time is 57 s, while for the lower nozzle the residence time is 45 s. The residence time is higher for the upper nozzle since not only do the particles have to travel a greater distance, but they are also more susceptible to collide with other particles easily changing the trajectory.

Figures 19, 20 and 21 present plots of particle diameter, moisture content and temperature of particles, respectively, as a function of residence time for a stream of particles with an initial diameter of 90 µm. By analysing the profiles at the same time it is possible to identify the different phases of the CDC model. Initially the droplet undergoes a temperature reduction until it reaches the wet bulb temperature, since it is above it. The first stage then begins and lasts until 0.75 s. This stage is charaterized by a constant temperature in which all the energy consumed due to convection is given over to evaporation, and by the reduction of moisture content to the critical point, X_{cr} = 0.61, where shrinkage of particle diameter stops. The second stage occurs from 0.75 s to 1.25 s, for a moisture content below to the critical until it reaches the equilibrium.

The different profiles follow closely the expected behaviour during the drying process of a droplet, confirming that the model describes accurately the process.

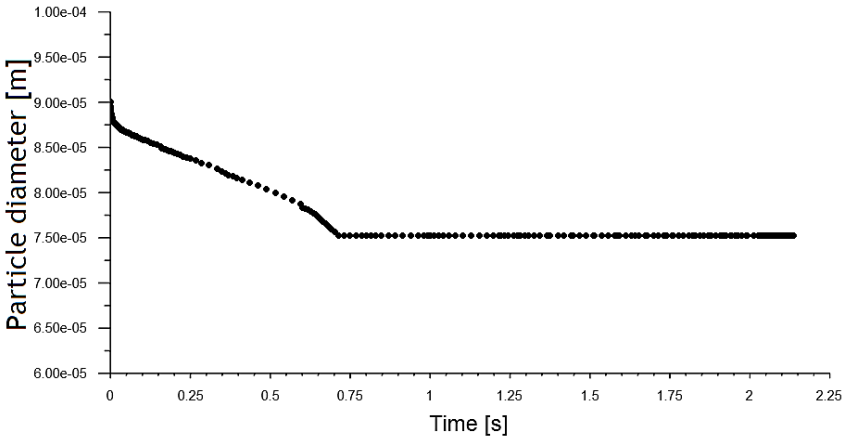

Figure 19 Particle diameter [m] as a function of residence time [s] (d_i = 90 µm).

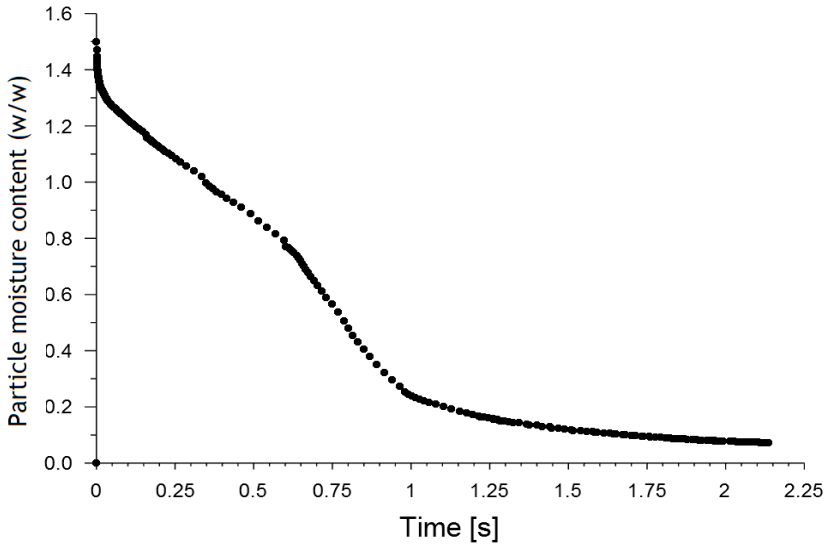

Figure 20 Particle moisture content (w/w) as a function of residence time [s] (d_i = 90 µm).

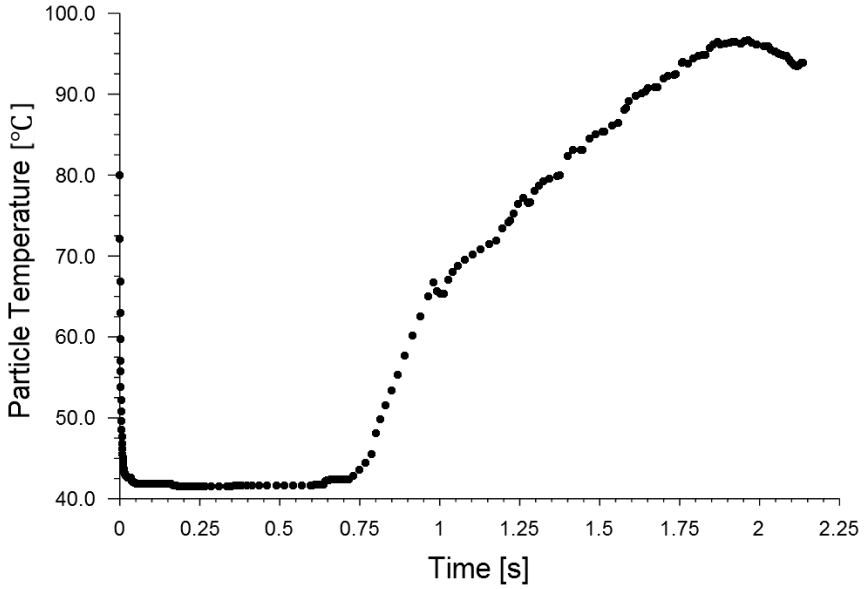

Figure 21 Particle temperature [ºC] as a function of residence time [s] (d_i = 90 µm).

In order to determine the possible agglomeration zones, the developed UDF allowed to obtain contours in the drying chamber that defined agglomeration areas. Figure 22 shows the possible areas where agglomeration can occur for a selected time, t = 80 s, considering that agglomeration occurs for three different cases:

- Case I: $\Delta T = (T_p - T_g) > 5$ ºC
- Case II: $\Delta T = (T_p - T_g) > 10$ ºC
- Case III: $\Delta T = (T_p - T_g) > 15$ ºC

The differences between each case are marked with a black line. Although the literature suggests that agglomeration occurs for a temperature difference above 10 ºC, the results indicate that agglomeration also occurs for a temperature difference of 5 ºC for maltodextrin DE12.

Observing agglomeration profiles, it can be seen that maltodextrin DE12 particles exhibit a sticky behaviour mostly on the region located at the bottom where the air has a higher temperature, velocity and lower moisture content. In these conditions particles start to caramelize and get sticky, causing agglomeration.

The changes in agglomeration zones from case to case are not easily visible. The biggest difference is noticed when comparing essays with different flow rates. For higher flow rates, as in essays A and C, agglomeration can occur in more regions. This could be related to the elevated number of collisions as the flow rate is higher. However, for this dissertation collisions are not considered when determining whether agglomeration is formed or not. Another explanation has to do with the higher kinetic energy transported by higher flow rates, that causes particles to be more often recycled inside the tower.

In the upper nozzle, at the spray region, particle agglomeration does not occur. This has to do with the higher moisture content of the particles, making this area more suitable for coalescence to happen. Although not as noticeable, agglomeration also does not happen in the spray region for the lower nozzle. However, temperatures are so high in this zone that evaporation occurs quickly, lowering the moisture content and subsequently raising particle temperature, resulting in favourable conditions for agglomeration near this region. For lower temperatures in the chamber, more wet particles will move to the bottom, so less agglomeration is expected in essay C.

Agglomeration will always occur for this type of material. However, depending on the initial conditions, this phenomenon can be minimized or increased, affecting the quantity of agglomerates formed. Considering the simulation results, there are more potential agglomeration zones for higher flow rates.

Particle agglomeration at different times was studied and can be seen in Figure C- 5, Appendix C. Changes in agglomeration are related to air movement.

It is important to note that this model does not take into account the temperature to which the particles stop being sticky and therefore stop agglomerating. Furthermore, it is assumed that whenever the moisture content is lower than critical, agglomeration occurs. However, it is known that experimentally the formation of agglomerates will also depend on impact angle and momentum. Otherwise, it is expected that there wouldn't be as many agglomeration regions as the simulation predicted.

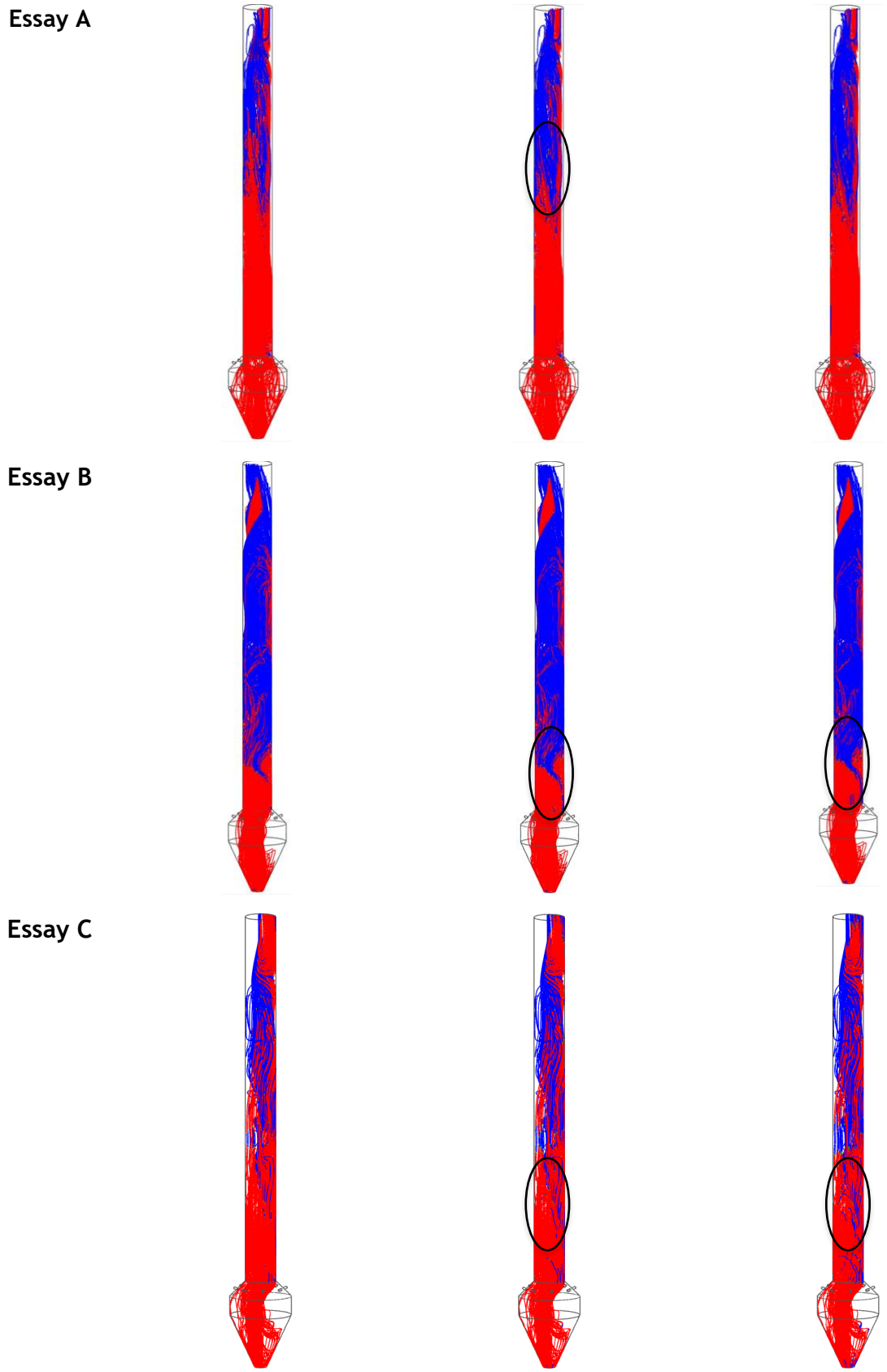

Figure 22 Agglomeration zones for different cases determined for t = 80 s in the spray dryer with differences marked by a black line (blue colour: non-agglomeration, red colour: agglomeration).

Photographic records of the powder product sorted by size for different essays can be seen in Figure 23.

By analysing laboratory samples of the powder product, visual confirmation of agglomeration in essay A and C was found. It was not possible to obtain photographic records for Essay B.

It is visible that essay A shows evidence of agglomeration, due to its size when compared to pure maltodextrin. The yellowish colour indicates that the material has reached a temperature that has incited it to caramelise and become sticky, initiating a degradation process. Essay C has a whiter colour more characteristic of pure maltodextrin, but it is also slightly more yellow and has larger particles. The difference in temperatures for the essays explains the colour discrepancy. Although along the tower the temperatures are similar, at the bottom they are much higher in essay A, causing the degradation of the particles. In essay C the agglomeration occurs at lower temperatures, keeping the original colour of the particles since the temperature is not high enough to degrade them.

Pure Maltodextrin DE12

Essay A

Essay C

Figure 23 Samples of the powder product for different essays.

Given that the accuracy of the particle temperature computation has been confirmed and that agglomeration has been visually verified, it might be possible to identify agglomeration zones by observing variations in T_g. However, simulation is carried out with several approximations from the reality. Thus, this model does not dispense the experimental validation by means of microscopical tests.

In addition to agglomeration, coalescence was also studied. It was assumed that for a moisture content higher than critical, coalescence would happen. This is a simplification of reality since, as discussed in section 2.2.4, coalescence is not solely dependent on moisture content. Results can be seen in Figure 24.

As expected, coalescence is formed in the spray region, confirming that there is no agglomeration in these regions. It can also be seen that for test C, it presents more regions where coalescence can form, due to the low inlet temperature.

Most of the particles that have coalesced and escaped through the top in the simulation will in the experimental process follow a downward path as the weight increase after coalescence causes the particles to move quickly to the lower zones of the tower.

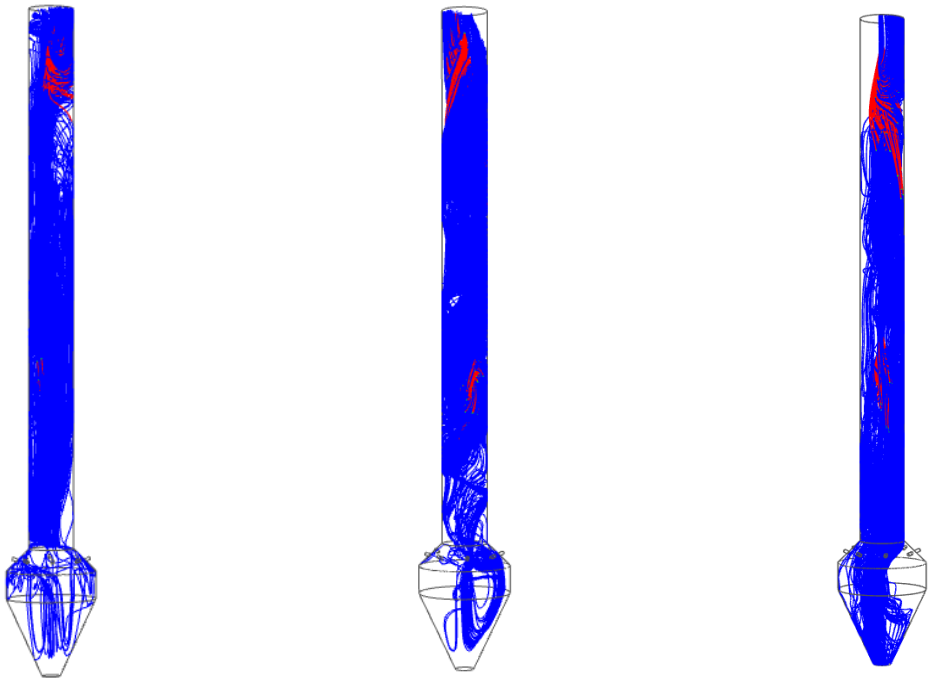

Essay A Essay B Essay C

Figure 24 Coalescence profiles in the drying chamber for different essays for t = 80 s.

The developed model does not take into consideration the effect of agglomeration and coalescence on the flow after droplets/particles merge, due to the difficulty of describing collisions in the DPM model. As a result, the model is a simplification of the actual experiment. Nevertheless, the experimental validation of the model will enable more understanding of these events.

5 Conclusions

Numerical CFD simulation of a counter-current spray dryer powered by two nozzles was performed in transient state in order to determine particle agglomeration zones for a 40 % (w/w) aqueous maltodextrin solution DE12.

For this purpose, adequate models were implemented on the Ansys Fluent program, using UDF functions, in order to describe spray drying process. DPM model was implemented to track particle's location as well as their properties. Particles moisture content evolution was determined applying the CDC model. The last model to be implemented was the Gordon-Taylor equation that gives information about the glass transition temperature (T_g) of the particles. Then, a relation between T_g and the sticky temperature was established. By analysing these temperatures, the proposed CFD modelling approach allowed the prediction of possible agglomeration zones during counter-current spray drying.

Studying velocity and temperature fields revealed the flow's instability in the geometry. The comparison between the radial temperature profiles obtained experimentally and computed using CFD are similar, allowing the accurate estimation of particle temperature. It was found that maltodextrin DE12 is more prone to agglomerate at the bottom of the chamber where temperatures are higher, and humidity is lower. For higher flow rates there are more areas prone to create agglomeration. If inlet temperatures are too high, the product starts to degrade and develops a yellowish powder colour.

Despite visual confirmation of agglomeration for some essays, this model requires experimental validation using microscopy analysis. Nevertheless, the developed agglomeration model allows a better understanding on the counter-current process and its complex flow. This model can be used as an engineering tool in order to optimise the already existing towers in terms of product quality or to design new spray drying systems for specific product characteristics.

For future studies the agglomeration model must be validated with experimental results.

6 Assessment of the work done

6.1 Objectives Achieved

The following objectives were achieved:

- Learn how to use CFD methods to simulate a spray dryer process.
- Get acquainted with the theoretical basis of spray drying process and methods of modelling drying in dispersed systems.
- Learn the basics of Ansys Fluent software and methods of modifying the program code using UDF functions in C language.
- Determine particle agglomeration zones during counter current spray dryer using CFD simulation.

6.2 Other Work Carried Out

Besides agglomeration phenomenon, possible coalescence areas were also determined.

6.3 Final Assessment

The development of this dissertation allowed me to acquire knowledge about new subjects, namely with spray dryer equipment, as well as Ansys CFD software and the writing of UDF code using C language.

Except for the experimental validation of the agglomeration model, due to problems in the laser system, all the objectives initially foreseen were accomplished.

7 References

Adhikari, B., Howes, T., Lecomte, D., & Bhandari, B. R. (2005). A glass transition temperature approach for the prediction of the surface stickiness of a drying droplet during spray drying. *Powder Technology*, *149*(2–3), 168–179. https://doi.org/10.1016/j.powtec.2004.11.007

Ali, M. (2014). *Numerical Modelling of a Counter-Current Spray Drying Tower*. *March*. https://core.ac.uk/download/pdf/29030463.pdf

Ali, M., Mahmud, T., Heggs, P. J., Ghadiri, M., Bayly, A., Ahmadian, H., & Juan, L. M. De. (2015). CFD simulation of a counter-current spray drying tower with stochastic treatment of particle-wall collision. *Procedia Engineering*, *102*, 1284–1294. https://doi.org/10.1016/j.proeng.2015.01.259

Ansys, F. (2020). *Module 01: Overview of the CFD Process Introduction to ANSYS Fluent*.

Borde, M. M. A. L. I. (2010). Theoretical Models of Single Droplet Drying Kinetics : A Review. *Drying Technology*, *October 2015*. https://doi.org/10.1080/07373930903530337

Dahiya, P., Caggioni, M., & Spicer, P. T. (2016). Arrested coalescence of viscoelastic droplets: polydisperse doublets. *Philosophical Transactions of the Royal Society A: Mathematical, Physical and Engineering Sciences*, *374*(2072). https://doi.org/10.1098/RSTA.2015.0132

Ferziger, J. H., & Peric, M. (2002). *Computational Methods for Fluid Dynamics* (3rd ed.). Springer-Verlag.

Frías, J. M., Oliveira, J. C., & Schittkowski, K. (2001). Modeling and parameter identification of a maltodextrin DE 12 drying process in a convection oven. *Applied Mathematical Modelling*, *25*(6), 449–462. https://doi.org/10.1016/S0307-904X(00)00060-3

Gecim, G., & Kalemtas, A. (2021). Processing and applications of ceramic microspheres. *Advanced Welding and Deforming*, 615–646. https://doi.org/10.1016/B978-0-12-822049-8.00020-7

Gianfrancesco, A., Turchiuli, C., Flick, D., & Dumoulin, E. (2010). CFD Modeling and Simulation of Maltodextrin Solutions Spray Drying to Control Stickiness. *Food and Bioprocess Technology*, *3*(6), 946–955. https://doi.org/10.1007/s11947-010-0352-2

Haider, A., & Levenspiel, O. (1989). Drag coefficient and terminal velocity of spherical and nonspherical particles. *Powder Technology*, *58*(1), 63–70. https://doi.org/10.1016/0032-5910(89)80008-7

Hashemi, N., Milani, E., Mortezavi, S. A., & Yazdi, F. T. (2017). Sticky point temperature as a suitable method in evaluation of shelf life of food powders. *Bulletin de La Société Royale Des Sciences de Liège*, *86*, 7–12. https://doi.org/10.25518/0037-9565.6519

Hong, L., Lee, C. F., & Huang, Y. J. (2016). *Statistical Mechanics and Kinetics of Amyloid Fibrillation*. https://doi.org/10.1142/9789813202382_0004

IPC Dresden. (n.d.). *Agglomeration - IPC Dresden EN*. Retrieved June 25, 2022, from https://www.ipc-dresden.de/agglomeration-59.html

Jaskulski, M. (2015). *CFD Modeling of Particle Agglomeration in Counter-Current Spray Drying Process*.

Jaskulski, M., Wawrzyniak, P., & Zbiciński, I. (2018). CFD simulations of droplet and particle agglomeration in an industrial counter-current spray dryer. *Advanced Powder Technology*, *29*(7), 1724–1733. https://doi.org/10.1016/j.apt.2018.04.007

Jin, Y., & Chen, X. D. (2009). Numerical study of the drying process of different sized particles in an industrial-scale spray dryer. *Drying Technology*, *27*(3), 371–381. https://doi.org/10.1080/07373930802682957

Jubaer, H., Afshar, S., Xiao, J., Chen, X. D., Selomulya, C., & Woo, M. W. (2019). On the effect of turbulence models on CFD simulations of a counter-current spray drying process. *Chemical Engineering Research and Design*, *141*, 592–607. https://doi.org/10.1016/j.cherd.2018.11.024

Kudra, T., & Strumillo, C. (1998). *Thermal processing of bio-materials*. Gordon and Breach Science Publishers.

Launder, B. E., & Spalding, D. B. (1974). The numerical computation of turbulent flows. *Computer Methods in Applied Mechanics and Engineering*, *3*(2), 269–289. https://doi.org/10.1016/0045-7825(74)90029-2

Lechler. (2022). *Pneumatic atomization*. https://www.lechler.com/de-en/technology/basics-nozzle-technology/atomization-methods/pneumatic-atomization

Malafronte, L., Ahrné, L., Innings, F., Jongsma, A., & Rasmuson, A. (2015). Prediction of regions of coalescence and agglomeration along a spray dryer-Application to skim milk powder. *Chemical Engineering Research and Design*, *104*, 703–712. https://doi.org/10.1016/j.cherd.2015.10.011

Ozmen, L., & Langrish, T. A. G. G. (2002). Comparison of glass transition temperature and sticky point temperature for skim milk powder. *Drying Technology*, *20*(6), 1177–1192. https://doi.org/10.1081/DRT-120004046

Pycia, K., Juszczak, L., Gałkowska, D., Witczak, M., & Jaworska, G. (2016). Maltodextrins from chemically modified starches. Selected physicochemical properties. *Carbohydrate Polymers*, *146*, 301–309. https://doi.org/10.1016/J.CARBPOL.2016.03.057

Razmi, R., Jubaer, H., Krempski-Smejda, M., Jaskulski, M., Xiao, J., Chen, X. D., & Woo, M. W. (2021). Recent initiatives in effective modeling of spray drying. *Drying Technology*, *39*(11), 1614–1647. https://doi.org/10.1080/07373937.2021.1902344

Siccama, J. W., Pegiou, E., Zhang, L., Mumm, R., Hall, R. D., Boom, R. M., & Schutyser, M. A. I. (2021). Maltodextrin improves physical properties and volatile compound retention of spray-dried asparagus concentrate. *LWT-Food Science and Technology*, *142*, 111058. https://doi.org/10.1016/j.lwt.2021.111058

Siemons, I., Politiek, R. G. A., Boom, R. M., van der Sman, R. G. M., & Schutyser, M. A. I. (2020). Dextrose equivalence of maltodextrins determines particle morphology development during single sessile droplet drying. *Food Research International*, *131*(November 2019), 108988. https://doi.org/10.1016/j.foodres.2020.108988

Simutech Group. (2022). *Top 5 Do's & Dont's for CFD (Computational Fluid Dynamics) | SimuTech*. https://simutechgroup.com/top-5-dos-donts-for-cfd/

Verdurmen, R. E. M., Menn, P., Ritzert, J., Blei, S., Nhumaio, G. C. S., Sonne Sørensen, T., Gunsing, M., Straatsma, J., Verschueren, M., Sibeijn, M., Schulte, G., Fritsching, U., Bauckhage, K., Tropea, C., Sommerfeld, M., Watkins, A. P., Yule, A. J., & Schønfeldt, H. (2004). Simulation of agglomeration in spray drying installations: The EDECAD project. In *Drying Technology* (Vol. 22, Issue 6). https://doi.org/10.1081/DRT-120038735

Verdurmen, R. E. M., van Houwelingen, G., Gunsing, M., Verschueren, M., & Straatsma, J. (2006). Agglomeration in spray drying installations (the EDECAD project): Stickiness measurements and simulation results. *Drying Technology*, *24*(6), 721–726. https://doi.org/10.1080/07373930600684973

Wawrzyniak, P., Jaskulski, M., Zbiciński, I., & Podyma, M. (2017). CFD modelling of moisture evaporation in an industrial dispersed system. *Advanced Powder Technology*, *28*(1), 167–176. https://doi.org/10.1016/j.apt.2016.09.029

Woo, M. W. (2016). *Computational fluid dynamics simulation of spray dryers An engineer's guide* (1st Editio). CRC Press.

Woo, M. W., Daud, W. R. W., Mujumdar, A. S., Talib, M. Z. M., Hua, W. Z., & Tasirin, S. M. (2008). Comparative study of droplet drying models for CFD modelling. *Chemical Engineering Research and Design*, *86*(9), 1038–1048. https://doi.org/10.1016/j.cherd.2008.04.003

Zbicinski, I., & Piatkowski, M. (2009). Continuous and Discrete Phase Behavior in Countercurrent Spray Drying Process. In *Drying Technology* (Vol. 27, Issue 12, pp. 1353–1362). https://doi.org/10.1080/07373930903383661

Annex A – Thickness layer calculations

Equations (A.1) – (A.6) were used to determine first layer thickness and equations (A.7) – (A.10) were used to determine the number of layers (Ansys, 2020).

First it is necessary to determine the Reynolds number (*Re):*

$$Re = \frac{\rho v L}{\mu} \tag{A.1}$$

where *ρ* is the fluid density, v is the velocity of the fluid, *L* is the characteristic length of the geometry and *μ* the dynamic viscosity.

The skin friction coefficient (c_f), for turbulent flow, is calculated using the Reynolds number in the following correlation:

$$c_f = 2log_{10}Re^{-0.65} - 2.3 \tag{A.2}$$

The wall shear stress (τ_w) can then be computed from the skin friction as:

$$\tau_w = \frac{1}{2}\rho v^2 C_f \tag{A.3}$$

Having computed the wall shear stress, the friction velocity (u_τ) can then be calculated using:

$$u_\tau = \sqrt{\frac{\tau_w}{\rho}} \tag{A.4}$$

The distance of the cell from the wall (y_P) is given by:

$$y_P = \frac{\mu y^+}{\rho u_\tau}, \tag{A.5}$$

where y^+ is the dimensionless distance from the wall and in the first calculation is an estimate.

Finally, the height of the first boundary layer is double of y_P:

$$y_H = 2y_P \tag{A.6}$$

Since y^+, initially, is estimated, it means that the first cell height is only a value without meaning that will need to be updated using y^+ obtained from the initial CFD analysis.

In order to determine *N* it is necessary to calculate the thickness of the laminar sublayer (δ) using Blasius solution:

$$\delta = \frac{4.91\ L}{\sqrt{\mathrm{Re}}} + \frac{0.38\ L}{Re^{1/5}} \tag{A.7}$$

Considering that each element of the boundary layer is 20 % (G = 1.2) higher than the previous one, the total thickness of the laminar sublayer can be expressed as a geometric sequence:

$$\delta = y_H + y_H G + y_H G^2 + \cdots + y_H G^{N-1} \tag{A.8}$$

The sum of the previous sequence can be written the following way:

$$\delta = y_H \frac{1 - G^N}{1 - G} \tag{A.9}$$

Rearranging the equation in order to N, allows to determine the number of layers:

$$N = \frac{\log\left(\frac{\delta(G-1)}{y_H} + 1\right)}{\log(G)} \tag{A.10}$$

Appendix A - UDF code

```
/*****************************************************************************
UDF for defining the heat and mass transport for multicomponent particle
vaporization
*****************************************************************************/
#include "udf.h"
#include "dpm_mem.h"
#include "math.h"
#include "surf.h"
#include "dpm.h"
#define x_cr 0.61                              /* value taken from MJ PhD*/
#define xs 0.4
#define x_m 0.0518
#define con_c 10.866
#define con_k 0.971


real H2O_Saturation_Pressure(real T)
{
real pot;
real psat;
if (T-273.15<100)
       {
       pot = pow(10,(8.07131-(1730.63/(233.426+(T-273.15))))); /* T in °C, P in mmHg
*/
       }
else
       {
       pot = pow(10,(8.14019-(1810.94/(244.485+(T-273.15)))));
       }
psat = 133.3223 * pot; /* from mmHg to Pa */
return psat;
}



DEFINE_DPM_HEAT_MASS(multivap,tp,Cp,hgas,hvap,cvap_surf,Z,dydt,dzdt)
{
 int ns;
 Material *sp;
 real dens_total = 0.0;                                    /* total vapor
density*/
 real P_total = 0.0;                                       /* vapor pressure */
 int nc = TP_N_COMPONENTS(tp);                             /* number of particle
components */
 Thread *t0 = TP_CELL_THREAD(tp);                          /* thread where the
particle is in - in which cell */
 Material *gas_mix = THREAD_MATERIAL(DPM_THREAD(t0, tp));  /* gas mixture
material - in that cell where particle is */
 Material *cond_mix = TP_MATERIAL(tp);                     /* particle mixture
material */
 cphase_state_t *c = &(tp->cphase[0]);                     /* cell information
of particle location */
 real molwt[MAX_SPE_EQNS];                                 /* Molecular weight
of gas species */
 real Tp = TP_T(tp);                                   /* Particle temperature */
 real mp = TP_MASS(tp);                    /* particle mass */
 real molwt_bulk = 0.;                     /* average molecular weight in bulk gas */
 real Dp = DPM_DIAM_FROM_VOL(mp / TP_RHO(tp));              /* particle diameter */
```

```
 real dpp = TP_USER_REAL(tp,2);
 real Ap = DPM_AREA(dpp);                                    /* particle surface */
 real f = TP_USER_REAL(tp,1);
 real Pr = c->sHeat * c->mu / c->tCond;                      /* Prandtl number */
 real Nu = 2.0 + 0.6 * sqrt((tp->Re)*dpp/Dp) * pow(Pr, 1./3.); /* Nusselt number */
 real h = Nu * c->tCond / dpp;                          /* Heat transfer coefficient */
 real dh_dt = h * (c->temp - Tp) * Ap;                  /* Heat source term - to know
how many energy we are using */



 dydt[0] += dh_dt / (mp * Cp);
 dzdt->energy -= dh_dt;
 mixture_species_loop(gas_mix,sp,ns)
 {
      molwt[ns] = MATERIAL_PROP(sp,PROP_mwi);  /* molecular weight of gas species*/
      molwt_bulk += c->yi[ns] / molwt[ns];     /* average molecular weight */
 }

/* prevent division by zero */
molwt_bulk = MAX(molwt_bulk,DPM_SMALL);

for (ns = 0; ns < nc; ns++)
  {
     int gas_index = TP_COMPONENT_INDEX_I(tp,ns);           /* gas species index of
vaporization */

  if(gas_index >= 0)
   {
        Material *cond_c = MIXTURE_COMPONENT(cond_mix, ns); /* Condensed material */
        real vap_temp = MATERIAL_PROP(cond_c,PROP_vap_temp);   /* vaporization
temperature */
        real D = DPM_BINARY_DIFFUSIVITY(tp,cond_c,TP_T(tp));   /* diffusion
coefficient */
        real Sc = c->mu / (c->rho * D);                        /* Schmidt number */
        real k  = (2. + 0.6 * sqrt((tp->Re)*dpp/Dp) * pow(Sc, 1./3.)) * D / dpp; /*
Mass transfer coefficient */
        real cvap_bulk = c->pressure / UNIVERSAL_GAS_CONSTANT / c->temp * c-
>yi[gas_index] / molwt_bulk / solver_par.molWeight[gas_index];  /* bulk gas
concentration (ideal gas) */
        real vap_rate = f*k * molwt[gas_index] * Ap * (cvap_surf[ns] - cvap_bulk);
/* Vaporization rate*/

        /* no vaporization below vaporization temperature, no condensation */
        if (Tp < vap_temp || vap_rate < 0.0)
            vap_rate = 0.;

        dydt[1+ns] -= vap_rate;
        dzdt->species[gas_index] += vap_rate;
        dydt[0] -= hvap[gas_index] * vap_rate / (mp * Cp); /*dT/dt = dh/dt/(m Cp) */
        dzdt->energy += hgas[gas_index] * vap_rate;   /* gas enthalpy source term */

        P_total += cvap_surf[ns];
        dens_total += cvap_surf[ns] * molwt[gas_index];
    }
    }
 }

DEFINE_DPM_SCALAR_UPDATE(new_variables,c,t,init,tp)
{
    int ns;
    int nc = TP_N_COMPONENTS(tp);

    real xw0 = 1-xs;                                  /* initial water mass fraction */
```

```
    real mp0 = TP_INIT_MASS(tp);              /* particle initial mass */
    real mp = TP_MASS(tp);                    /* particle mass */
    real wap_mass, xv, xi, f, dp, Tg;

    real xeq, humi, coal, agl1, agl2, agl3, vapMassFrac;

    real Tp = TP_T(tp)-273.15;                /* Particle temperature */
    real Tgs = 153;                           /* Tg pure maltodextrin */
    real Tgw = -135;                          /* Tg pure maltodextrin */
    real k = 0.22;                            /* solid-water binary constant */
      real stPres = H2O_Saturation_Pressure(C_T(c,t));      /* saturated vapour
pressure for water */


    if (init)
    {
        TP_USER_REAL(tp,0) = mp0*xw0/(mp0-(mp0*xw0));     /* moisture content per
dry weight - gravimetric moisture content */
        TP_USER_REAL(tp,1) = 1;
        TP_USER_REAL(tp,2) = TP_INIT_DIAM(tp);
        TP_USER_REAL(tp,3) = 1;
      /*coalescence */
            TP_USER_REAL(tp,4) = 20;          /*Tg */
        TP_USER_REAL(tp,6) = 0;               /*difference 1 */
            TP_USER_REAL(tp,7) = 0;           /*difference 2 */
            TP_USER_REAL(tp,8) = 0;           /*difference 3 */
            TP_USER_REAL(tp,9) = 0;
            C_UDMI(c,t,0) = 0;
            C_UDMI(c,t,1) = 0;
            C_UDMI(c,t,2) = 0;
      }
    else
    {

        for (ns = 0; ns < nc; ns++)
        {

            int gas_index = TP_COMPONENT_INDEX_I(tp,ns);
                if (ns == gas_index)
                {
                    xv = TP_COMPONENT_I(tp,ns);           /* mass fraction of
evaporated water */
                    wap_mass = mp*xv;                     /* mass of water */
                    xi = wap_mass/(mp-wap_mass);          /* mass of water per mass
of dry dry solid - moisture content on dry basis  */
                                vapMassFrac = C_YI(c,t,ns);
                           /* water mass fraction in air */
                    humi = ((C_P(c,t)+101325)*vapMassFrac)/stPres;    /* air
relative humidity in particle cell */

                                if (humi > 1.0) {humi = 1;}
                                else {humi =
((C_P(c,t)+101325)*vapMassFrac)/stPres;}     /* in case if there will be numerical
error in cell */

                                xeq = (x_m*con_c*con_k*humi)/((1-
con_k*humi)*(1+(con_c-1)*con_k*humi));       /* GAB sorption isotherm */

                    Tg = ((1 - xv) * Tgs * k + xv * Tgw) / ((1 - xv) * k + xv);

                                if (xi >= x_cr)

                    {
                        f = 1.0;
```

```
                        dp = TP_DIAM(tp);
                        coal = 1;
                        agl1 = 0;
                        agl2 = 0;
                        agl3 = 0;
                         }

                    else
                    {
                                        if (xi-xeq <= 0.0) {f = 0.0;}    /* no
evaporation and condensation below xeq */
                                        if (x_cr-xeq <=0.0){f = 1.0;}
                                        else
                                        {
                                        f = pow((xi-xeq)/(x_cr-xeq), 3.22);
                        dp = TP_USER_REAL(tp,2);
                        coal = 0;

                                        }
                        if (Tp - Tg >= 5)
                                                        {agl1 = 1;}
                           else         {agl1 = 0;}
                                  if (Tp - Tg >= 10)
                                                        {agl2 = 1;}
                           else         {agl2 = 0;}
                                  if (Tp - Tg >= 15)
                                                        {agl3 = 1;}
                            else        {agl3 = 0;}
                    }

                }
          }
        }

              TP_USER_REAL(tp,0) = xi;
              TP_USER_REAL(tp,1) = f;
              TP_USER_REAL(tp,2) = dp;
              TP_USER_REAL(tp,3) = coal;
              TP_USER_REAL(tp,4) = Tg;
              TP_USER_REAL(tp,6) = agl1;                        /* difference 1 */
              TP_USER_REAL(tp,7) = agl2;                        /* difference 2 */
              TP_USER_REAL(tp,8) = agl3;                        /* difference 3 */
              TP_USER_REAL(tp,9) = xeq;

              C_UDMI(c,t,0) = TP_USER_REAL(tp,6);
              C_UDMI(c,t,1) = TP_USER_REAL(tp,7);
              C_UDMI(c,t,2) = TP_USER_REAL(tp,8);
}
```

Appendix B – Distribution ring

Table B- 1 provides a comparison between measured and CFD simulation temperatures inside connection ducts for the mesh with 482k hexagonal elements for different inlet conditions.

Table B- 1 Measured temperatures [℃] inside connection ducts and CFD simulation results for different inlet conditions.

No. duct	Essay A Temperature / ℃		Essay B Temperature / ℃		Essay C Temperature / ℃	
	Measured	CFD	Measured	CFD	Measured	CFD
1	-	223.3	-	199.1	-	184.2
2	-	239.78	-	228.0	-	195.4
3	-	245.3	-	243.2	-	199.8
4	-	234.6	-	232.7	-	197.0
5	240	232.4	240	234.4	185	196.1
6	-	239.2	-	241.5	-	197.4
7	-	237.6	-	237.1	-	194.2
8	-	231.7	-	225.7	-	189.1

Appendix C – Drying chamber

Boundary conditions

Table C- 1 presents the inlet boundary conditions at the connection ducts in the drying chamber for the different essays.

Table C- 1 Inlet boundary conditions at connection ducts in the drying chamber.

	Essay A		Essay B		Essay C	
Duct №	**T / ℃**	$\dot{m}$ **/ kg s^{-1}**	**T / ℃**	$\dot{m}$ **/ kg s^{-1}**	**T / ℃**	$\dot{m}$ **/ kg s^{-1}**
1	223.3	0.00679	199.1	0.00678	184.2	0.00680
2	239.8	0.00658	228.0	0.00658	195.4	0.00663
3	245.3	0.00650	243.2	0.00649	199.8	0.00655
4	234.6	0.00662	232.7	0.00661	197.0	0.00662
5	232.4	0.00664	234.4	0.00663	196.1	0.00663
6	239.2	0.00662	241.5	0.00662	197.4	0.00665
7	237.6	0.00665	237.1	0.00664	194.2	0.00669
8	231.7	0.00676	225.7	0.00675	189.1	0.00679

Heat Losses

Table C-2 lists the values for the calculated heat transfer coefficient (α_p), theoretical heat flux, and obtained by CFD simulation for different essays.

Table C- 2 Values of heat transfer coefficient, theoretical and CFD simulation heat flux for different essays.

Essay	α_p **/ W m^{-2} K^{-}**	**Heat Flux / W m^{-2}**	
		CFD	**Theoretical**
A	3.43	691	532.2
B	2.32	470	350.4
C	2.68	450	333.82

Radial temperatures in the chamber

Figure C- 1 displays the predicted gas temperature profile and the measured time-averaged temperature profile along the radial coordinate for different window levels and different essays.

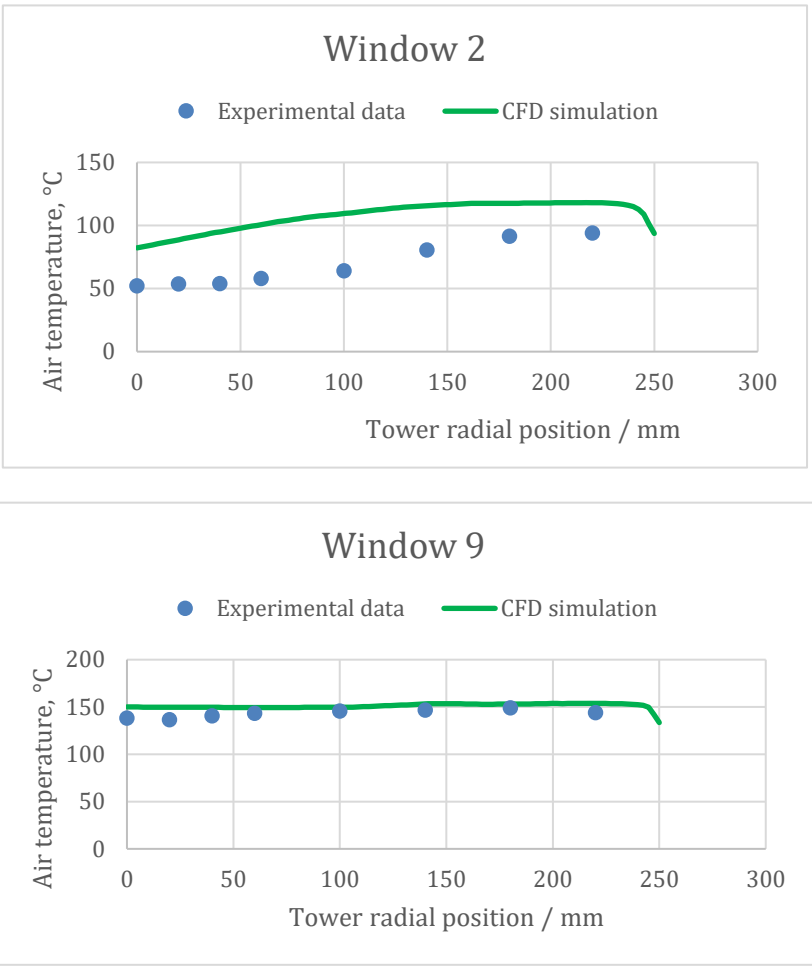

Figure C- 1 Profiles of mean air temperature [ºC] along the radial position [mm] for different windows height determined using CFD and obtained experimentally for Essay A.

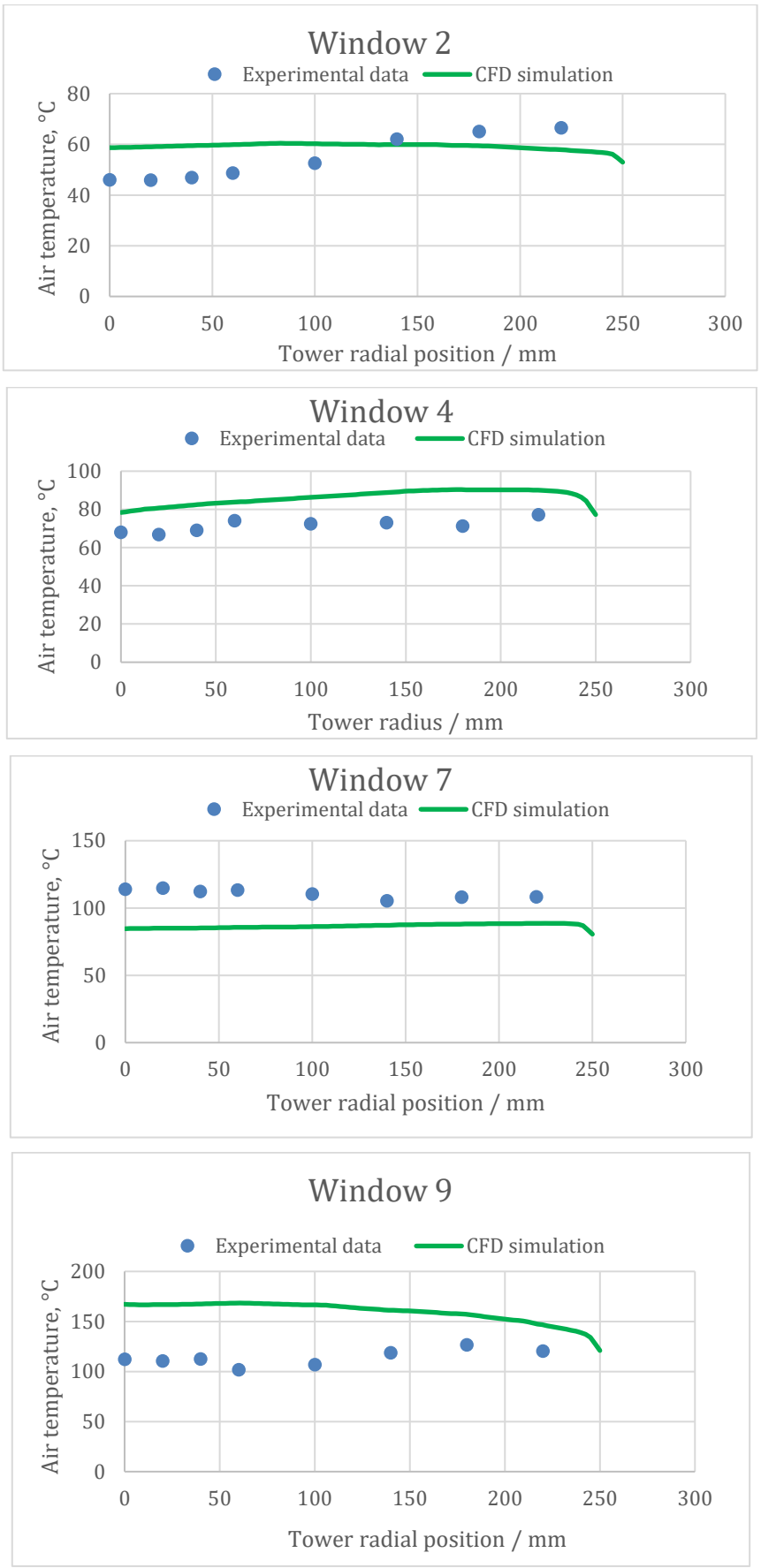

Figure C- 2 Profiles of mean air temperature [ºC] along the radial position [mm] for different windows height determined using CFD and obtained experimentally for Essay B.

Continuous phase velocity

Figure C- 3 is a vector plot of air velocity for essay A at t = 80 s where it can be observed the changes in velocity direction along the drying chamber.

Figure C- 3 Air velocity vectors in axial cross-section of the drying chamber for t = 80 s (blue colour: upward airflow, red colour: downward airflow).

Particle trajectories

Some examples of individual stream's trajectories are presented in Figure C- 4.

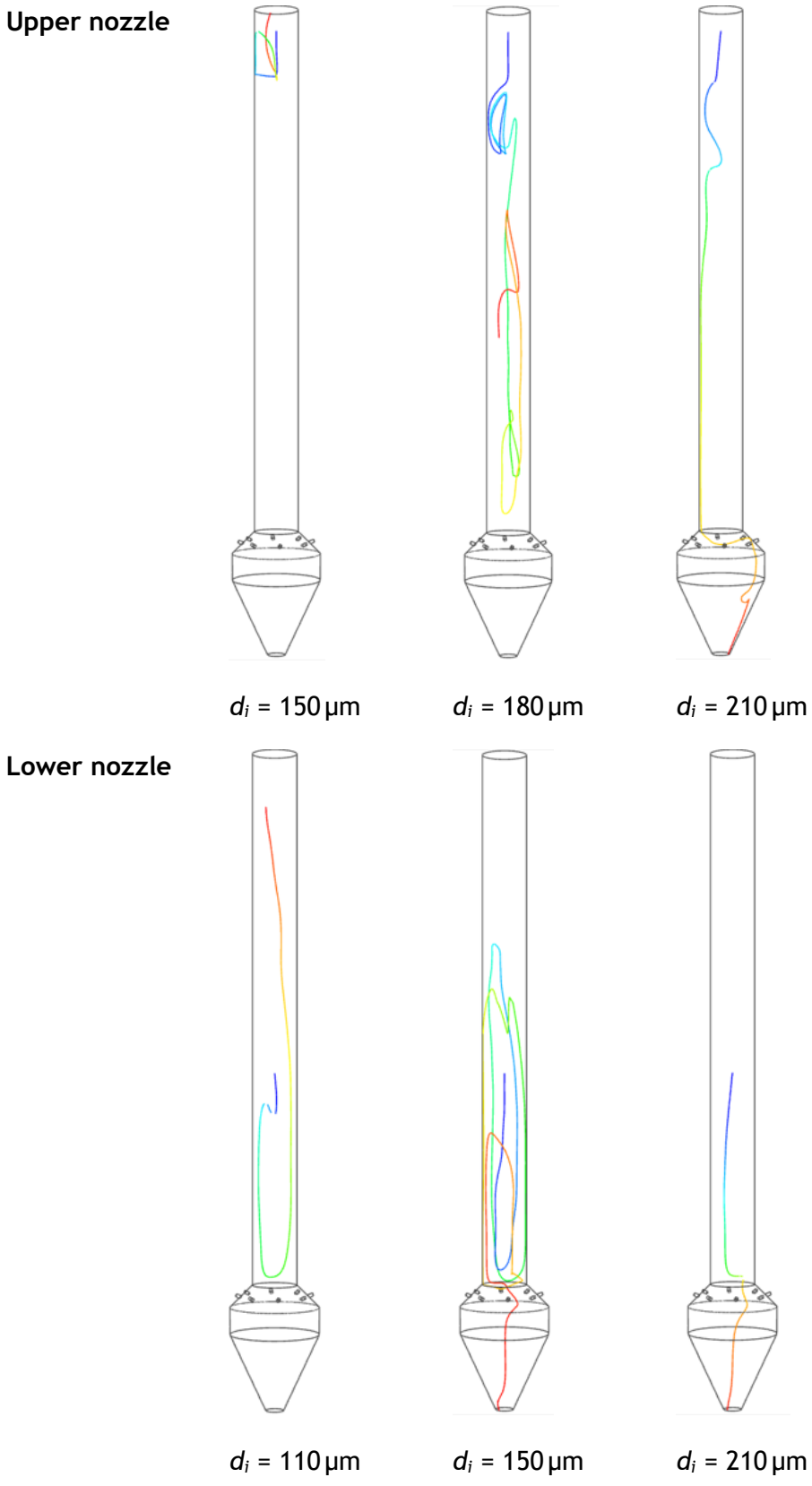

Figure C- 4 Individual particle trajectories for distinct stream diameters from upper and lower nozzles.

Agglomeration

Particle agglomeration at consecutive times for essay A can be observed in Figure C- 5.

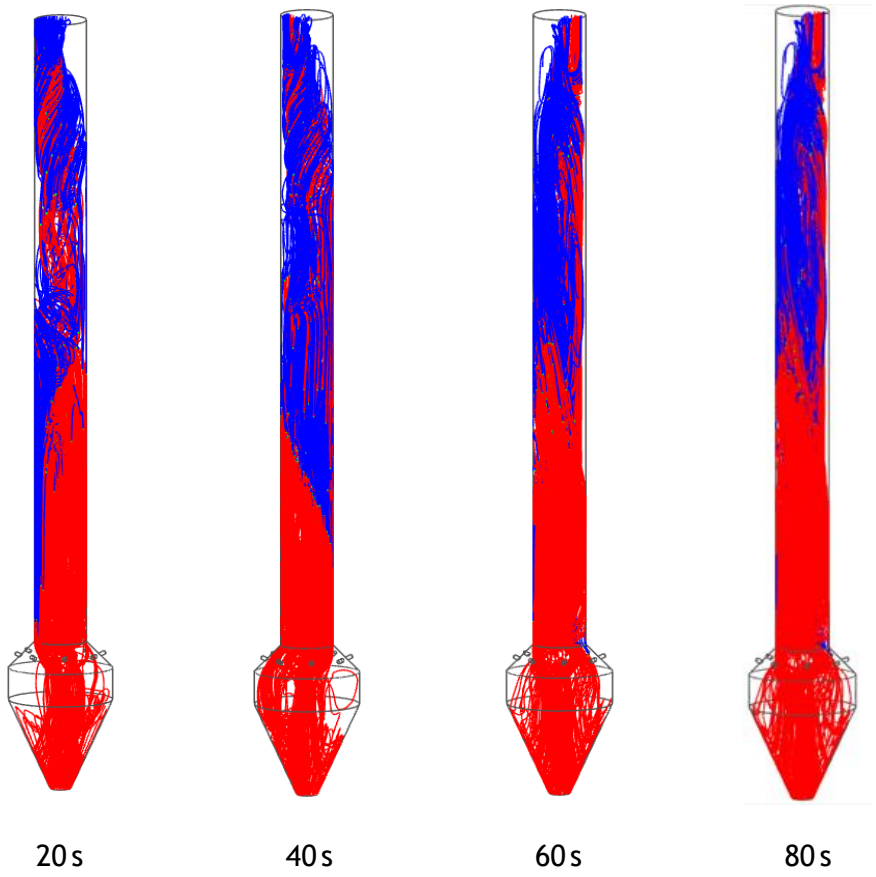

Figure C- 5 Particle agglomeration for different times inside the drying chamber (red colour: agglomeration, blue colour: non agglomeration).